Chapter 8
Atmospheric Transport Schemes: Desirable Properties and a Semi-Lagrangian View on Finite-Volume Discretizations

Peter H. Lauritzen, Paul A. Ullrich and Ramachandran D. Nair

Abstract This chapter has twofold purpose. After a short introduction to the mass continuity equations in atmospheric models, desirable properties for mass transport schemes intended for meteorological applications are discussed in some detail. This includes a discussion on the complications caused by the non-linearity of most problems of interest that makes it hard to define accuracy and convergence as the 'truth' is not known. Thereafter, some finite-volume schemes from the atmospheric literature are reviewed and discussed. To complement the large existing literature on finite-volume schemes, a less frequently discussed semi-Lagrangian derivation of the finite-volume method is given that focuses on 'remap-type' schemes where the space and time discretizations are combined rather than separated. A discussion on the challenges in deriving accurate schemes intended for global models and non-traditional spherical grids is given as well.

P.H. Lauritzen
National Center for Atmospheric Research[†], 1850 Table Mesa Drive, Boulder, CO 80305, USA, e-mail: pel@ucar.edu
[†]The National Center for Atmospheric Research is sponsored by the National Science Foundation.

P.A. Ullrich
University of Michigan, 2455 Hayward St., Ann Arbor, MI 48109, USA, e-mail: paullric@umich.edu

R.D.Nair
National Center for Atmospheric Research, 1850 Table Mesa Drive, Boulder, CO 80305, USA, e-mail: rnair@ucar.edu

8.1 Introduction

To predict the evolution of air and tracers[1] we solve one of the fundamental laws of physics namely the equation of mass continuity. This equation is intuitively very simple to understand; perhaps the simplest statement of the equation is that mass of air and tracers is conserved without the presence of sources or sinks. Hence mass in a volume can only change if there is inflow and/or outflow through surfaces bounding the closed volume or if there are parameterizised sources and/or sinks (e.g., for water vapor, sources and sinks can be evaporation and condensation, respectively)

$$\frac{d}{dt}\left(mass\right) = inflow - outflow + sources - sinks. \tag{8.1}$$

The continuity equation is simple, in a strict mathematical sense, and it may appear as a surprise that we use an entire chapter discussing it. However, despite its simplicity finding an accurate and efficient numerical approximation to its solution remains an active research subject and no scheme to date is ideal (and perhaps never will be as long as computing power remains finite). Also, the continuity equation is coupled to the other equations of motion, so a complete discussion of the challenges in air and tracer transport must also consider this coupling. The purpose if this chapter is to convey some of the many deliberations in transport scheme development and to discuss some examples of transport schemes on the sphere.

In the literature there are numerous review articles and books on transport methods in general and specifically on the finite-volume method (e.g., Rood, 1987; LeVeque, 1996) and this chapter is not an attempt to supersede or replace these reviews. Instead we shall limit the review to space-time (or remap) finite-volume transport schemes used in meteorology. By space-time schemes we refer to schemes where the temporal and spatial discretizations are combined rather than separated. As will become clear one may also refer to space-time (or remap) schemes as *cell-integrated* (or *finite-volume*) *semi-Lagrangian* schemes. Conservative grid-to-grid interpolation (also referred to as remapping), which is usually an integral part of finite-volume schemes, will also be discussed in some detail. Obviously this chapter will only scratch the surface of the enormous literature on transport schemes and we will emphasize the intuitive (and perhaps more physical) derivation of schemes rather than mathematical rigor.

The chapter is organized as follows. Before diving into the nuts and bolts of finite-volume schemes we begin by formulating the transport problem relevant to atmospheric models (section 2) and discuss some desirable properties that transport schemes intended for atmospheric applications ideally should possess (section 3). In section 4 the mathematical foundation for space-time finite-volume schemes is given in Eulerian and Lagrangian forms. The equivalence between the two forms is rarely discussed but useful in gaining more understanding of Eulerian schemes. In section 5 the spatial and temporal approximations needed for practical schemes

[1] a tracer in this context is any quantity that follows the flow of air such as chemical species and water in the atmosphere

are presented step by step. This includes upstream cell approximation, sub-grid-cell reconstruction and practical integration over cells in space. Section 5 is mostly limited to two-dimensional schemes on the Cartesian plane, however, a brief discussion on the extension to spherical geometry is given. In section 6 we discuss the extension to three dimensions. Before the final remarks in section 8 some practical considerations for the coupling of transport schemes to the continuity equation for air are discussed in section 7. This includes the inconsistencies that may arise in the air mass and tracer mass coupling, techniques for sub-cycling the air mass equation with respect to tracers, and coupling a semi-implicit air mass scheme with an explicit tracer mass scheme (section 7). For brevity, section 6 and 7 are cursory while more attention will be given to desirable properties and the space-time scheme derivations on the plane.

8.2 The continuous equation

8.2.1 Representation of mass in atmospheric models

Most atmospheric models have at least a handful of continuity equations and, in most cases, many more. From a dynamics point of view the continuity equation for air is the most fundamental and important continuity equation since it is strongly coupled to the momentum equations and the thermodynamic equation. For the representation of moist processes most models have prognostic continuity equations for three water species: Water vapor, cloud liquid water and cloud ice water. Some high resolution models also have resolved-scale continuity equations for rain and snow (if there is no resolved-scale continuity equation for rain and snow the assumption is usually that rain and snow falls to the ground in one time-step). Modern micro-physical parameterizations include prognostic continuity equations for four to eight condensed species. For example, the Morrison and Gettelman (2008) micro-physics package used in NCAR's Community Atmosphere Model (CAM) version 5 has continuity equations for mass and number concentrations for ice and liquid water. Some microphysics parameterizations also have prognostic continuity equations for mass and number concentrations for ice and liquid precipitation. Modal (and even more for bin) aerosol schemes may have 20 or more prognostic continuity equations for mass and number concentrations of aerosols such as particulate organic matter, dust, sea salt, secondary organic aerosols, number concentrations for different sizes of aerosols, etc. In addition, any prognostic representation of chemical species requires the solution to one continuity equation per species e.g. MOZART (Model of Ozone And Related Tracers, Brasseur et al 1998). So needless to say, the continuity equations make up a dominant part in atmospheric models at least in terms of the total computational cost of the dynamical core[2].

[2] roughly speaking the *dynamical core* is the part of the model that solves the governing fluid and thermodynamic equations on resolved scales (Thuburn, 2008)

First, let us discuss the representation of air mass in atmospheric models as this has fundamental influence on how all other species are treated. The density of well-mixed moist air ρ_m can be separated into a dry and wet part

$$\rho_m = \frac{m_d + m_v}{V} = \rho_d + \rho_v = \rho_d + q_v \rho_m, \tag{8.2}$$

where m_d and m_v are the masses of the dry air and water vapor, respectively, and V is a small volume. The density of dry air and water vapor are denoted ρ_d and ρ_v, respectively, and q_v is the specific humidity,

$$q_v = \frac{m_v}{m_d + m_v}. \tag{8.3}$$

To a very good approximation the mass of dry air is the mass of the dominant well-mixed gases: Nitrogen N_2 (ca. 78.0.8%), Oxygen O_2 (ca. 20.95%), Argon Ar (ca. 0.93%) and Carbon dioxide CO_2 (at present ca. 0.038%). These gases make up over 99.998% of the volume of dry air and may therefore be considered permanent (although argon and carbon-dioxide are slowly increasing). In addition, small amounts of trace gases are mixed into the air (with sources and sinks varying in space and time), however, the variation in these 'non-permanent' gases is very small compared to the total mass of all the trace gases. Trenberth and Smith (2005) estimated that the dry air mass of the atmosphere corresponds to a surface pressure of approximately 983.05 hPa and it varies less than 0.01 hPa based on changes in atmospheric composition. So the variation in the dry air mass budget is on the order of 0.001%. So to a very good approximation the continuity equation for dry air does not have any source or sink terms, and thus reads

$$\frac{\partial \rho_d}{\partial t} + \nabla \cdot (\rho_d \mathbf{v}) = 0, \tag{8.4}$$

where $\mathbf{v}$ is the velocity field and '$\nabla\cdot$' is the divergence operator. The mass of dry air accounts for approximately 99% of the total mass of atmosphere and the remaining 1% is approximately the mass of water vapor. The continuity equation for humidity (water vapor) is given by

$$\frac{\partial}{\partial t}(\rho_m q_v) + \nabla \cdot (\rho_m q_v \mathbf{v}) = P_{q_v \rho_m}, \tag{8.5}$$

where $P_{q_v \rho_m}$ represents sources and sinks (in this case condensation and evaporation processes). Moisture q_v varies significantly (relatively speaking) with values near zero for cold dry air and a few percent in warm moist air. The continuty equation for moist air can be obtained by adding (8.4) and (8.5), and using (8.2) to simplify. The result is

$$\frac{\partial \rho_m}{\partial t} + \nabla \cdot (\rho_m \mathbf{v}) = P_{\rho_m}. \tag{8.6}$$

This equation is similar to the equation for dry air (8.4) except for the humidity forcing terms.

The prognostic variables used for tracers are usually defined in terms of mixing ratios. If moist density is prognosed, the mixing ratios for tracers are most conveniently defined in terms of the specific concentration

$$q_m^{(l)} = \frac{m^{(l)}}{m_d + m_v}, \tag{8.7}$$

where $m^{(l)}$ is the mass of constituent (l). So the density of the constituent is $\rho^{(l)} = q_m^{(l)} \rho_m$, where $q_m^{(l)}$ is the 'moist' mixing ratio. However, one may also solve the continuity equation for tracers in terms of the 'dry' mixing ratio $q_d^{(l)}$, defined by

$$q_d^{(l)} = \frac{m_d^{(l)}}{m_d}. \tag{8.8}$$

As discussed in Collins et al (2004) the advantage of using (8.7) is that the mass of species (l) is obtained by simply multiplying the moist mixing ratio with the moist air density $q_m^{(l)} \rho_m$. However, this approach has the disadvantage of implicitly requiring a change in $q_m^{(l)}$ whenever the water vapor q_v changes. This disadvantage does not exist if (8.8) is used.

8.2.2 Consistency in the mass equations

Herein we will respectively use ρ and q to denote air density and mixing ratio (which can be either moist or dry) and we assume no sources or sinks (no forcing terms). Then the two-dimensional continuity equation for air density ρ can be written as

$$\frac{\partial \rho}{\partial t} + \nabla \cdot (\rho \mathbf{v}) = 0, \tag{8.9}$$

and similarly for a tracer density ρq

$$\frac{\partial (\rho q)}{\partial t} + \nabla \cdot (\rho q \mathbf{v}) = 0, \tag{8.10}$$

where $\mathbf{v}$ is the velocity vector. Note that (8.9) and (8.10) imply

$$\frac{dq}{dt} = 0, \quad \frac{d}{dt} \equiv \frac{\partial}{\partial t} + \mathbf{v} \cdot \nabla, \tag{8.11}$$

which states that q is conserved along trajectories/characteristics of the flow. Note that the continuity equations (8.9) and (8.10) are linked in the sense that ρ appears in both equations. Hence, numerical error introduced in simulating the evolution of air mass ρ may be reflected in the prognosed trace gas mixing ratios when converting from tracer mass ρq to mixing ratio q.

To solve any of the continuity equations given above the flow field **v** must be given. The continuity equation for air (8.9) is coupled with the momentum equations and thermodynamic equations. Hence the thermodynamic variables and other prognostic variables feed back on the velocity field which, in turn, feeds back on the solution to the continuity equation. It follows that the continuity equation for air cannot be solved in isolation and one must obey the maximum allowable time-step restrictions imposed by the fastest waves in the system[3] (see chapter 1 and 6). The passive tracer transport equation (8.10) or (8.11) can be solved in isolation given prescribed winds and air densities, and is therefore not susceptible to the stricter time-step restrictions imposed by the fastest waves in the system but 'only' to the less restrictive advective velocities[4]. Hence, if for stability relatively short time-steps must be used for the continuity equation for air, one does not necessarily need to use short time-steps for the tracers (at least not for stability reasons). That is, one can solve the tracer transport equations with time-steps longer than what are allowed for stability in (8.9). This technique is referred to as *sub-cycling*, that is, multiple cycles of dynamics (air continuity equation) are performed within one time-step of the tracers. In doing so care must be taken to retain the consistency between tracers and air. For example, if $q = 1$ then (8.10) reduces to (8.9) and additional care must be taken to ensure consistency between these equations in the discretization. Specific examples and details on sub-cycling are given later (section 8.7.2). First, let us consider important design objectives for tracer transport schemes intended for atmospheric applications.

8.3 Desirable properties

When developing a new transport (or any other) algorithm one is usually striving for a scheme that ensures simulation *veracity*. In other words, a numerical method should be designed so that simulations using it are as truthful as possible. In mathematical literature simulation *veracity* is often synonymous with accuracy which is associated with the absolute truth. Convergence, truncation error and error norms are all associated with quantitative measures of conformity to the truth. In most realistic atmospheric model settings, however, the truth is unknown in an absolute sense (the exact solution is not known). For instance, in most atmospheric applications an increase in resolution will often resolve finer scales and new phenomena appear making it problematic to define convergence in a strict mathematical sense. Adding to the complexity is the fact that the system is chaotic and therefore not deterministic beyond 10 days or so (Lorenz, 1982), so any attempt to assess absolute accuracy in simulations beyond the predictability limit must be based on statistical approaches.

[3] assuming that explicit time-stepping is used

[4] although there is a weak coupling between humidity and the thermodynamic/momentum equation

In all, simulation veracity in an atmospheric modeling context is more than accuracy in a strict mathematical sense. Perhaps because there is little quantitative knowledge of the true solution a lot of emphasis is placed on physical properties of the solution method. For example, we do know that the numerical solution should ideally obey discretized equivalents of properties we can derive from the continuous set of equations such as conservation[5] of mass and higher moments, shape-preservation (including monotonicity, positivity and non-oscillatory property), correlation preservation, and so on. Also, sub-grid-scale parameterizations usually require physical realizable atmospheric states from the resolved scale dynamics. From a computational point of view properties such as parallel efficiency, geometric flexibility, etc. are also very important properties of the final numerical algorithm.

What follows is a list of desirable properties for tracer transport schemes that are all (apart from the properties related to efficiency) essential ingredients of simulation veracity:

8.3.1 Accuracy (error norms)

Accuracy describes the degree of closeness of the simulated (numerically computed) solution to its true (exact) state specified in terms of error norms (numeric values). The error measures can either be assessed at a fixed resolution (absolute error) or as a function of resolution (convergence). For linearized equations and approximations a proxy for convergence can be sought by computing the formal order of accuracy of the numerical method through Taylor series expansions. Note that formal order of accuracy does not necessarily guarantee accurate solutions for distributions/flows with near discontinuities (shocks and fronts) nor does it guarantee accuracy at a particular resolution. For many global weather and climate applications absolute accuracy at a particular range of resolutions is perhaps more important than high-order convergence rates. Below is a list of some idealized test cases used to quantitatively assess simulation veracity:

8.3.1.1 Linear test cases

Error norms are well defined when the exact solution is known which is usually only the case for linear problems. Commonly used linear test cases, where the analytical solution is known at all times t, can be divided into two categories: Translational and deformational. Here we focus only on global test cases in spherical geometry.

Most test cases are formulated with non-divergent flow fields for which the advective form of the continuity equation for a tracer (8.11), that uses mixing ratio q as the prognostic equation, is equivalent to the flux-form version (8.10) based on tracer mass ρq. That is, q or ρq is set equal to the same spatial distribution and the modeler

[5] for a discussion on conservation in the context of the full equation set for the atmosphere see chapter 11

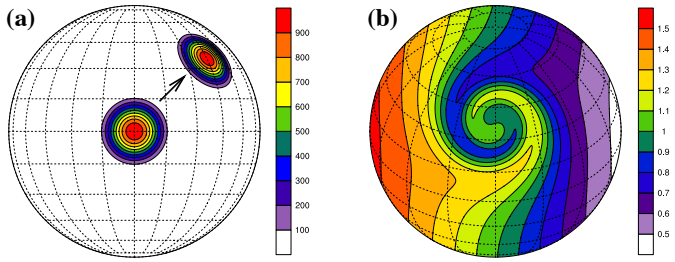

Fig. 8.1 Exact solutions for the (a) solid body advection of a cosine bell test case at $t = 0$ (center of plot) and $t = 44$h (for a 'flow rotation angle' of 45°), and (b) the static vortex test case at day 6.

is implicitly assuming that ρ is one everywhere and since the flow is non-divergent ρ will remain one through-out the simulation at least in the analytical case. Hence the modeler is not forced to distinguish between tracer mass ρq and mixing ratio q. However, for a divergent/convergent flow only q is constant along parcel trajectories whereas tracer mass ρq will increase/decrease in areas of convergence/divergence. For a fuller discussion see Nair and Lauritzen (2010).

Translational. Probably the most commonly used idealized test case in the meteorological literature is the solid body rotation of a cosine bell (Figure 8.1a) (e.g., test case one of the widely used two-dimensional test suite of Williamson et al 1992 for the shallow-water equations). The exact solution is simply the translation of the initial condition and standard error norms can be computed at every time-step. This two-dimensional test case has been extended to three dimensions in Jablonowski et al (2010). Another three dimensional test case on the sphere where the analytic solution is known was proposed by Zubov et al (1999).

For convergence studies used to assess the formal order of accuracy of a scheme the translated distribution should be sufficiently smooth. For example, the cosine bell distribution may appear smooth but it is only C^1 at the base of the bell. Consequently, schemes that are high-order accurate in terms of a Taylor Series analysis may not show this high-order formal convergence rate when using the cosine bell initial condition. To assess 'ideal' convergence rates it is advised to use C^∞ functions such as Gaussian surfaces (Levy et al, 2007).

Deformational. The translational test case described above has a large degree of symmetry and perhaps is not challenging enough to thoroughly test a numerical algorithm. Real world flows also have deformational, convergent/divergent and rotational components that deform, expand and rotate the initial distribution. A popular purely deformational test case (non-divergent) is the cyclogenesis test case introduced in meteorology by Doswell (1984) and used as a test case for transport schemes by numerious authors (e.g., Rančić 1992, Nair and Machenhauer 2002). The exact solution at day 6 is shown on Fig. 8.1b[6]. As can been seen in the Fig-

[6] the dimensionalization of the vortex problem used here follows Nair and Jablonowski (2008)

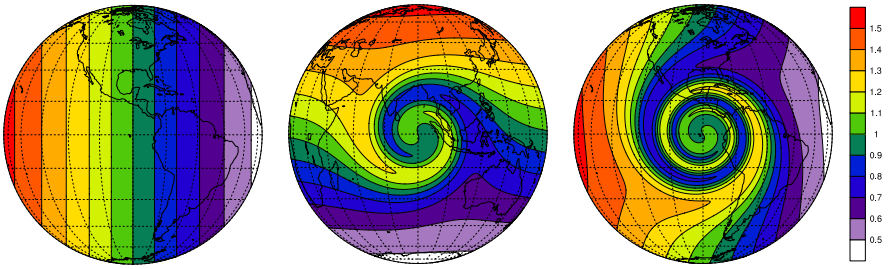

Fig. 8.2 Exact solutions for the moving vortex test case with a flow orientation of 45° at zero (left; day 0), half (middle; day 6) and one (right; day 12) revolution. The continents are shown for reference purposes only.

ure the vortex 'curls up' and generates long thin filaments in the process. These, in general, are quite challenging to represent for any numerical scheme.

Another useful application of this test case is to use its velocity field but instead of transporting an initial condition such as shown on Fig. 8.2 in the cyclogenesis test case, instead transport a constant mass field $\rho = \rho_0$. Since the flow is non-divergent any numerical scheme should ideally preserve a constant mass field. Also the solid-body rotation flow field is non-divergent and so for this wind field a constant mass-field should remain constant throughout the simulation. However, the cyclogenesis wind field is much more challenging as a preservation of constancy test since it is deformational (unless the stream function for the velocity field is used to makes sure that the divergence that the scheme 'sees' is zero). Some schemes might preserve a constant mass field for solid body advection but fail to preserve a constant mass field for the deformational wind field. Unfortunately results from such tests are rarely presented in the literature.

Translational and deformational. Although the idealized cyclogenesis test case described above is challenging it lacks a translational component. Nair and Jablonowski (2008) combined the cyclogenesis wind field with the solid body advection wind field on the sphere which makes up the 'moving vortices' test case. Instead of a stationary 'curl up' of the vortex, it is transported as a solid body as it deforms (Fig. 8.2). Obviously such a test case is more challenging and might therefore be more useful to discriminate between schemes than simpler test cases. For example, in the idealized tests of the finite-volume transport scheme in Lauritzen et al (2010) it was found that the moving vortices test case was more discriminating than the pure translational and stationary cyclogenesis test cases (at least when applied and compared to the Putman and Lin (2007) scheme).

Recently, Nair and Lauritzen (2010) extended LeVeque's test case (LeVeque, 1996) to a class of test cases on the sphere. Unlike all the test cases considered so far the wind fields in this test case are time varying. In these cases the wind fields are periodic and reverse so that after one period the initial distribution has returned to its initial position and shape. Hence the analytic solution is known after one period

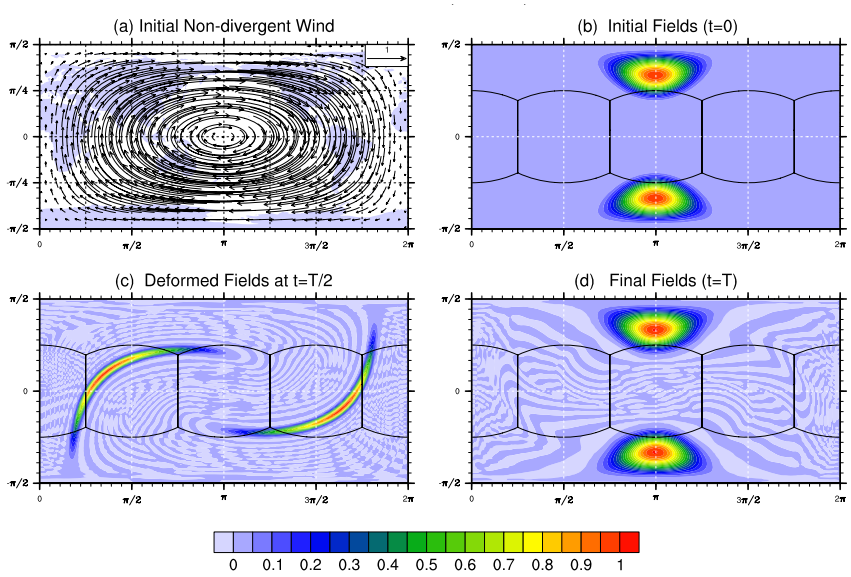

Fig. 8.3 The recently proposed test case by Nair and Lauritzen (2010). (a) The initial wind field and (b) initial condition and analytical solution after one period. (c) and (d) show a numerically computed solution after half and full period, respectively. The grid-scale noise in (c) and (d) are due to the numerical scheme not being monotone/shape-preserving.

but not throughout the simulation. The flow is swirling (deformational) so the initial condition is highly deformed half way through the simulation. This challenges the numerical scheme since grid-scale features develop from well-resolved initial conditions (Fig. 8.3). And perhaps more importantly, one of the test cases in Nair and Lauritzen (2010) is divergent contrary to most idealized test cases for transport on the sphere which are non-divergent. By introducing divergence the modeler is forced to distinguish between mixing ratio and air mass which is not strictly necessary for non-divergent test cases.

8.3.1.2 Non-linear test cases

In linear test cases for smooth flows the accuracy in terms of error norms is usually improved when the resolution is increased and when the formal order of the numerical method is increased. However, such idealized experiments do not truly quantify the error in realistic atmospheric applications that are far from linear. In general, for non-linear problems the quantification of error is problematic except in very simple cases[7] and, as discussed in Prather et al (2008), we usually design models with the expectation that a correct solution (truth) exists and that with adequate physical ap-

[7] e.g., the one-dimensional Burgers' equation that has an exact solution although it is non-linear

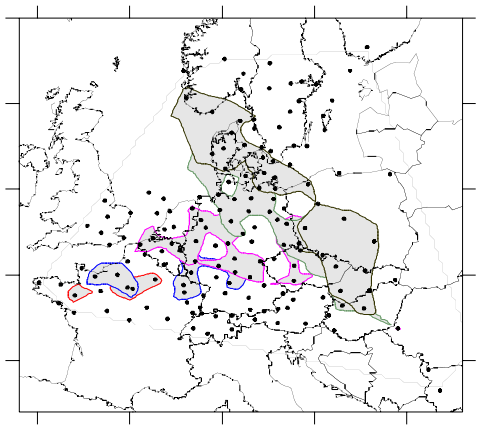

Fig. 8.4 The ETEX sampling stations distribution (filled black circles) and 0.1 ngm^{-3} contour of measured cloud at T_0+12 hours (red) ,+24 hours (blue), +36 hours (purple), +48 hours (green), +60 hours (black). Figure courtesy of Stefano Galmarini.

proximations and numerical methods our solutions will converge to a 'true' solution as the resolution is increased.

In the context of passive tracer transport a non-exhaustive list of non-linear test cases is given below. The examples are meant to give the reader an idea of the 'world' beyond idealized linear test cases that are usually reported on in transport scheme development. All test cases do not have analytical solutions and involve the solution to the entire system of dynamical equations (not just prescribed winds and mass-fields) as well as parameterizations of sub-grid-scale processes making it harder to distinguish numerical errors of the transport scheme from other sources of error.

The ETEX forecast experiment. The worst nuclear power plant disaster in history (the Chernobyl power plant explosion in 1986) generated a radioactive plume that drifted over extensive parts of western Russia and Europe. This is a rude reminder of the importance of having models capable of forecasting long-range transport accurately; at least for emergency management. As a consequence the European Tracer Experiment (ETEX, see, e.g., Girardi et al 1998, van Dop et al 1998 and the more recent study of Galmarini et al 2004) was established in 1994 to evaluate the validity of long-range transport models and to assemble a database which would allow the evaluation of long-range atmospheric dispersion models in general.

ETEX was a controlled experiment where two releases (under different weather conditions) of perfluorocarbon tracers from Western France were tracked across Europe. Perfluorocarbon tracers are non-depositing, non-water-soluble and inert, and therefore a passive tracer for all practical purposes. A large network of samplers deployed eastward on the territory of Central and Eastern Europe collected tracer samples that were later analyzed to determine the concentration levels. That set of

measurements was then used to quantitatively evaluate the predictions of the models.

The ETEX experiment and data can be used to evaluate new transport schemes. Obviously this test case indirectly tests more than the transport scheme itself but also parameterizations (such as boundary layer parameterizations, parameterized vertical diffusion etc.) and, in general, the models ability to produce accurate winds and air densities for the tracer transport scheme[8].

Mixing experiments. There are several experiments in the literature targeting the mixing properties of the model. Probably the simplest was proposed by Rasch et al (2006). The experiment is setup as follows. The mixing ratio for a tracer is set to one everywhere in a model layer and zero elsewhere. Then the model is run from some meteorological initial conditions for 30 days. The tracer is placed either near the surface (near 800 hPa) and around 200 hPa. The low tracer test serves as an indicator of transport in a region dominated by sub-grid scale transport processes such as convection and turbulence. The high tracer is much more dominated by resolved-scale dynamics at least at middle and high latitudes. The test case also indicates the tropospheric-stratospheric mixing in the model (generally, in the polar and mid-latitude regions stratospheric air is mixed into tropospheric air and in the Equatorial regions deep convection results in a large scale ascent of tropospheric air). For models based on an isentropic vertical coordinate, this test when run adiabatically and with non-zero tracer values in an isentropic layer instead of pressure levels, can be used to indicate the amount of spurious vertical diffusion in the transport scheme since ideally the mixing ratio should remain one in the isentrophic layer for all time (and zero elsewhere).

Another experiment that is probably more widely used is the age-of-air experiment (see, e.g., Waugh and Hall 2002 and references herein). The age of air is the mean transport time from some reference location. For example, stratospheric age of air is the mean transport time from the tropical tropopause to a location in the stratosphere. Monitoring the age of air for species with long lifetimes provides a proxy for the diffusivity (often spurious) of the tracer transport in a particular model. In general, schemes that are too diffusive tend to produce too 'young' air while less diffusive schemes simulate 'older' age of air. Eluszkiewicz et al (2000) found a large dependency on the choice of advection scheme in age-of-air experiments in addition to the simulated large scale simulation. Even for short-lived tracers with sources and sinks Rasch et al (2006) found a large dependency on the numerical solution technique. These studies demonstrate that the choice of transport scheme (and driving model) can easily influence the simulation at a level that can strongly modulate the physical signal of interest.

[8] there have been other controlled tracer transport experiments before ETEX, e.g., ANATEX (The Across north America Tracer Experiment) and CAPTEX (Cross-Appalachian Tracer Experiment) and also more recent experiments such as MEGAPOLI (Emissions, urban, regional and Global Atmospheric POLlution and climate effects, and Integrated tools for assessment and mitigation; http://megapoli.info).

Dynamics/tracer consistency. This test was proposed by D. Johnson (University of Wisconsin) and published in Rasch et al (2006). It targets the model's ability to simulate transport of conserved tracers consistently and the model's ability to maintain non-linear relationships between six different conserved and non-conserved tracers. It can be shown from the second law of thermodynamics that two points separated in space and time connected by a trajectory should satisfy a non-linear relationship in terms of temperature T, potential temperature θ and pressure p (see Appendix of Rasch et al 2006):

$$\theta_1 = \left(\frac{\theta_0}{T_0}\right) T_1 \left(\frac{p_0}{p_1}\right)^{R/C_p}, \tag{8.12}$$

where the subscript 0 and 1 refer to the two points, and R and C_p are the gas constant and specific heat constant at constant pressure, respectively. The test case consists of predicting θ, T and p^{R/C_p} separately and then check how well they obey (8.12). The level of agreement between these two ways of computing potential temperature yields a measure of the degree of consistency in the model. See Rasch et al (2006) for details. It is probably impossible to construct a scheme that will exactly fulfill this consistency test, however, it is desirable that schemes strive to be as consistent as possible.

8.3.2 Conservation of mass

As discussed in section 8.2.1 one of the most fundamental budgets of the global atmosphere is that for the mass of dry air. Since the physical variation in the dry air mass budget is on the order of 0.001% (and usually not modeled) even minor drifts in the dry air mass budget due do numerical errors would be larger than the physical variation in the dry air mass budget (Moorthi et al, 1995).

For the trace gases any spurious non-conservation of mass will effectively correspond to a spurious source or sink for the gas in question. In particular for long-lived trace species such as stratospheric ozone it is paramount that their mass-budgets are well maintained in the models. Even for highly reactive tracers such as reactive chlorine compounds, mass-conservation is important since the sum of all the compounds should be conserved although individual compounds have large sources and sinks (one compound is converted into another).

There are two ways of obtaining mass-conservation in numerical schemes. Either an inherently conservative numerical method is used or mass-fixers (see chapter 13) can be employed. For the mass of dry air mass-fixers usually operate by increasing or decreasing the mean of the pressure field (mass) by an amount corresponding to the spuriously lost or gained mass caused by the lack of conservation of the numerical method. Note that such a procedure can be done so that it does not alter gradients in the pressure field and was shown by Williamson and Olson (1994) to have mini-

mal effect on the simulation. Mass-fixers are applied in numerious non-conservative models, e.g., the spectral transform versions of NCAR's Community Atmosphere Model (CAM, Collins et al 2004). Although mass-fixers for the pressure field seem to not adversely affect simulations it is far more problematic to apply mass-fixers for tracers. For example, altering mixing ratios to obtain tracer mass-conservation can lead to unphysical large or small mixing ratios. If that is the case the mass-fixer must do a local adjustment and thereby it might introduce new extrema in the tracer mass fields and gradients are no longer preserved. This may also disrupt tracer correlations (tracer correlations are discussed in section 8.3.7 below) and consistency between tracer and air mass (see section 8.3.4 below). Therefore finite-volume methods that are inherently conservative, have become a popular numerical method in climate and chemistry modeling since *ad-hoc* adjustments are, in theory, not necessary[9].

The continuous equations of motion conserve all moments not just mass. However, Thuburn (2008) argued (see also chapter 11) it might not be desirable that the advection scheme also preserves higher-order moments.

8.3.3 Optimal diffusion and dispersion properties

The linear diffusion and dispersion properties of a linearized scheme can be assessed by performing a von Neumann stability analysis (also known as a Fourier stability analysis). It is a standard analytic analysis technique and is described in many textbooks in the context of grid-point methods (see, e.g., Durran 1999, Haltiner and Williams 1980) and in the context of finite-volume methods in Lauritzen (2007). The analysis consists of assessing analytically how a single Fourier mode is damped and accelerated/decelerated by the numerical scheme during one time-step assuming a constant wind field.

In one dimension the von Neumann analysis is performed by assuming a solution in the form

$$\psi^n(x) = \psi^0 \Gamma^n \exp(\hat{\imath}\kappa x), \tag{8.13}$$

where $\hat{\imath}$ is the imaginary unit, ψ^0 the initial amplitude, and $\kappa = 2\pi/L$ is the wavenumber (L is the wavelength), and n is the time-level index. The damping and phase properties of a scheme are assessed by substituting the solution (8.13) into the forecast formula for the finite-volume scheme in question, and subsequently analyzing the complex amplification factor Γ. The stability of a numerical method is governed by the modulus of the complex amplification factor, that is, a particular wave with wavenumber κ is stable if $|\Gamma| \leq 1$. Following Bates and McDonald (1982) the dispersion properties of a scheme is assessed by writing the complex amplification factor as

$$\Gamma = |\Gamma| \exp(-\hat{\imath}\omega^* \Delta t), \tag{8.14}$$

[9] we write 'in theory' since if a transport scheme is not strictly monotone local 'ad hoc' adjustments might be necessary even for finite-volume methods

where ω^* is the numerical frequency. Define the relative frequency as $R = \omega^*/\omega$ where ω is the exact frequency given by κu_0 and u_0 is the constant wind. If $R > 1$ the numerical scheme is accelerating and if $R < 1$ the scheme is decelerating compared to the exact solution.

The Von Neumann analysis provides useful information about the stability properties of a scheme and may provide new insight into schemes. The limitation of the von Neumann stability analysis is that it is linear. Hence any non-linear operators such as limiters and filters cannot be included in the basic analysis as well as non-linear flows. Usually the spurious numerical diffusion and dispersion decrease rapidly with the formal order of the scheme. So each scheme probably has an optimal order for which the extra computational cost associated with increasing the order of the scheme simply does not pay off in terms of linear diffusion and dispersion properties. For example, Leonard (1991) argued that the reduction in diffusion becomes trivial soon after the order is larger than third.

8.3.4 Tracer and air mass consistency

Tracer and air mass consistency is a stricter concept than simple mass conservation of the individual quantities. It basically states that the discretized tracer transport scheme should reduce to the discretized continuity equation for air when $q = 1$ as is the case for the continuous equations: (8.10) reduces to (8.9) when setting $q = 1$. Tracer-air mass consistency can, for example, be violated if using a numerical method for tracer transport that is different from the scheme used for predicting the evolution of the air density [10]. To achieve a high level of consistency it is usually necessary that the same numerical algorithm is used for the dynamics as well as for tracer transport. For more discussion see Machenhauer et al (2009); Lee et al (2004); Jöckel et al (2001); Zhang et al (2008).

8.3.5 Divergence preservation

The transport operator should not be a spurious source of divergence. Usually this property is discussed within the context of non-divergent flow fields. For example, a constant initial mass distribution should remain constant at all time in a non-divergent flow (*preservation of mass-constancy*). The subject has received considerable attention in the magnetohydrodynamics literature since the magnetic flux density is non-divergent and the numerical scheme should ideally retain that prop-

[10] This discussion applies to online applications where tracer transport is performed in conjunction with the governing fluid and thermodynamic equations. A similar inconsistency appears when driving the tracer transport equation in an offline mode (prescribed winds and mass fields from reanalysis, observations or a different model) in which case the tracer transport scheme with $q = 1$ will not equal the prescribed mass-field unless ad-hoc fixers are applied.

erty (e.g., Artebrant and Torrilhon (2008) and references therein). A prerequisite for controlling spurious generation of divergence is preservation of mass-constancy as formulated above (see test case suggestion in section 8.3.1.1) for non-divergent flows.

Note that the preservation of constant mixing ratio (and not constant tracer mass field) is trivial in most cases. If the advective form of the advection equation (8.11) is used it is trivial to maintain a constant mixing ratio since q is the prognostic variable and the divergence does not appear explicitly. If the air and tracer equations are solved on flux-form (equations (8.9) and (8.10), respectively) using the same numerical method, it is usually trivial to preserve a constant mixing ratio field since the mixing ratio q is recovered from (8.10) by dividing the prognosed tracer mass field ρq by ρ from (8.9). So even if the numerical scheme is unable to preserve a constant mass field ρ, it is usually possible to design schemes so that a constant q field is recovered when dividing $\rho\, q$ by the (potentially) non-divergence preserving forecast of ρ.

8.3.6 Physical realizability (monotone, positive-definite, non-oscillatory, shape-preserving)

In the absence of sources and sinks the mixing ratio of a Lagrangian parcel being transported by the flow is invariant (8.11). If the numerical solution fulfills this property it is *monotonicity*[11] *preserving*; no new local extrema are generated and the absolute values of pre-existing local extrema is non-increasing. Strict monotonicity preservation can be hard to achieve and enforcing it in numerical schemes is often found to be at the cost of overall accuracy wherefore it is often relaxed somewhat.

The zero-th order shape-preservation property is that the numerical scheme generates physically realizable solutions. Since mixing ratios cannot physically take negative values they should remain non-negative. Schemes that cannot generate negative values are termed *positive definite* and schemes that do not generate wiggles (spurious grid-scale waves as the ones on Fig.8.3c and d) typically associated with large gradients are referred to as *non-oscillatory*. Obviously a scheme that is monotone is automatically positive-definite and non-oscillatory but not necessarily vice versa. It should be stressed that it is q that should remain monotone and not $\rho\, q$. For convergent flows $\rho\, q$ can physically take values outside the range of the initial condition whereas q should not. See Nair and Lauritzen (2010) for a discussion and simple illustration of the latter for an idealized flow field.

Note that shape-preservation can be enforced in finite-volume schemes based on (8.9) and (8.10) if these schemes imply some discretized version of (8.11). Schemes that retain such a property are termed *compatible* (Schär and Smolarkiewicz, 1996).

[11] atmospheric modelers tend to be a bit loose with the term 'monotone' and normally they do not refer to the careful definition given by Harten (1983)

8.3.7 Preservation of pre-existing functional relations between species (correlations)

As described in Plumb (2007): "Relationships between long-lived stratospheric tracers, manifested in similar spatial structures on scales ranging from a few to several thousand kilometers, are displayed most strikingly if the mixing ratio of one is plotted against another, when the data collapse onto remarkably compact curves." In other words, different longlived trace constituents (such as nitrous oxide N_2O and 'total odd nitrogen' NO_y) seem to be related through rather simple functional relationships in, for example, the polar stratospheric vortex. Such relationships can arise from different reasons (Plumb and Ko, 1992), however, it is well-known that transport can establish such relations (e.g. Thuburn and Mclntyre, 1997).

In order to accurately simulate such relationships in numerical models, the transport operator should, at least, be able to preserve linear correlations (Lin and Rood, 1996; Thuburn and Mclntyre, 1997). That is, the transport operator should maintain the relationship in (8.15) throughout the simulation

$$q_1 = \gamma^{(0)} + \gamma^{(1)} q_2, \tag{8.15}$$

where $\gamma^{(i)}$, $i = 0, 1$, are constants, and q_i, $i = 1, 2$, are mixing ratios of two linearly interrelated species. A transport scheme will preserve linear pre-existing functional relations if the transport operator $\mathscr{T}$, that updates $q_i, i = 1, 2$, in time, is 'semi-linear'

$$\mathscr{T}(q_1) = \mathscr{T}\left(\gamma^{(0)} + \gamma^{(1)} q_2\right) = \gamma^{(0)}\mathscr{T}(1) + \gamma^{(1)}\mathscr{T}(q_2) = \gamma^{(0)} + \gamma^{(1)}\mathscr{T}(q_2), \tag{8.16}$$

(Lin and Rood, 1996; Thuburn and Mclntyre, 1997). As noted by Thuburn and Mclntyre (1997) the successful preservation of linear correlations by a transport operator does not necessarily gurantee an accurate solution since shaping two tracer fields the same way does not necessarily imply shaping them the right way. On the other hand, if a model significantly violates the preservation of linear correlations between chemical constituents, the model is most likely not going to provide truthful simulations of the relation between those constituents.

Since interrelated tracers can also be related non-linearly, it is also of interest to investigate how a transport operator distorts such non-linear relation. For example, consider two tracers that are initially correlated by a fourth-order polynomial

$$q_1 = \gamma^{(0)} + \gamma^{(1)} (q_2)^4, \tag{8.17}$$

(Thuburn and Mclntyre, 1997) where the constants $\gamma^{(0)}$ and $\gamma^{(1)}$ should be chosen so that the functional relation is either convex or concave in the range of the initial condition values of q_1 and q_2. Except for fully Lagrangian transport operators, schemes are usually unable to maintain non-linear functional relationships and their degree of non-preservation of correlations effectively translates into numerical mixing of the constituents. Initializing two tracers that are, for example, related through (8.17) and letting the tracers be transported by a challenging flow that de-

velops features that collapse to the near grid-scale, provides physical insight into the numerical mixing that the transport operator introduces (Thuburn and Mclntyre, 1997). No practical Eulerian and semi-Lagrangian scheme can preserve (8.17) and will therefore produce scatter points that deviate from the pre-existing functional relationship (8.17). When scatter points deviate from the pre-existing functional relation curve the transport operator is introducing numerical mixing. The numerical mixing can either be spurious or resemble 'real' mixing. If the scatter values are on the concave side of the pre-existing functional relation, the numerical mixing is similar to 'real mixing' that is observed in the atmosphere (see Fig. 8.5). Mixing in the atmosphere occurs, for example, when the polar stratospheric vortex breaks up (e.g. Waugh et al, 1997). If scatter values appear outside the 'convex hull' (either by producing scatter points on the convex side of the pre-existing functional relationship curve and/or outside the range of the initial condition for $q_i, i = 1, 2$), the model produces numerical unmixing which is unlike 'real mixing'. Thuburn and Mclntyre (1997) proved that in order to guarantee only 'real' numerical mixing, the transport operator should be 'semi-linear' and monotone according to Harten (1983). Unfortunately only first-order schemes will meet these requirements. Since first-order schemes are too diffusive for most atmospheric applications, one must accept some level of unmixing. For a more complete discussion of this topic the reader is referred to Thuburn and Mclntyre (1997). Recently, Lauritzen and Thuburn (2010) proposed mixing diagnostics that quantifies the amount of numerical mixing that the transport operator introduces for interrelated species.

Another situation relevant to the transport of chemical species is the situation in which more than two species are related through some complicated relation but they add up to a constant (or a smooth spatial field[12]). With just two species this reduces to preserving a linear correlation but with more than two species it is very challenging to guarantee that the total mixing ratio remains constant, except by transporting the total or using a fully Lagrangian scheme. The transport operators ability to maintain the constant sum is another measure for numerical mixing and has been explored in one dimension by Ovtchinnikov and Easter (2009). Note that maintaining or only perturbing pre-existing functional relations in a 'physical way' is not only important for long-lived stratospheric tracers but also for other parts and processes in the atmosphere such as cloud-aerosol interactions (Ovtchinnikov and Easter, 2009). In all, single-tracer testing that has traditionally been used to evaluate transport operators in idealized settings does not provide insight into how well tracer interrelations are maintained although it is important for many atmospheric applications.

[12] for example, total reactive chlorine in the stratosphere

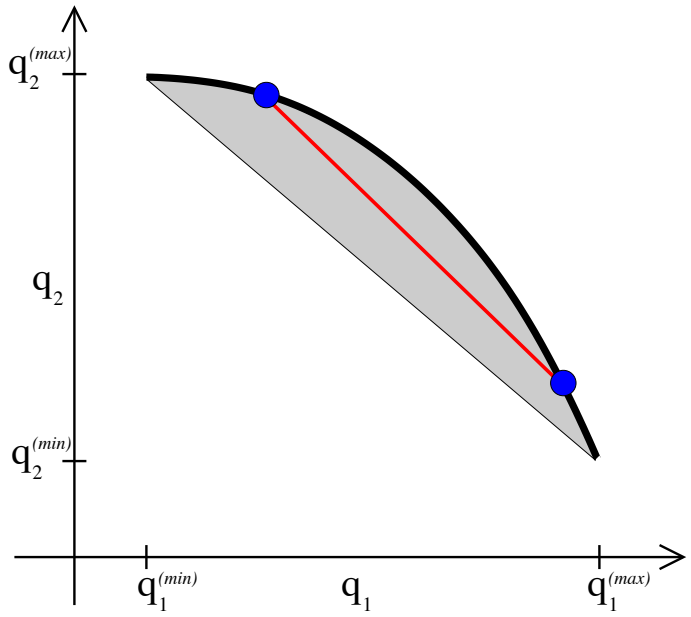

Fig. 8.5 Schematic view of the effect of mixing on a scatter plot where mixing ratio for tracer 1, q_1, is plotted against tracer 2, q_2. The two tracers are initially non-linearly correlated, that is, the scatter points (q_1, q_2) are on the pre-existing functional relation curve (solid thick line curve). The initial ranges for the two tracers are $[q_1^{(min)}, q_1^{(max)}]$ and $[q_2^{(min)}, q_2^{(max)}]$, respectively. Partial mixing of two air masses (two filled circles - scatter points) will tend to move the two scatter points towards each other along the straight (red) line (also referred to as a 'mixing line'). Hence 'real mixing' occurring in the atmosphere will tend to move points on the scatter plot to the concave side of the pre-existing functional relation curve (also referred to as the 'convex hull' - shaded area).

8.3.8 Robustness

The numerical method should remain stable and retain simulation veracity throughout the integration. Robustness can be assessed by testing the algorithm for many different flow fields, temporal and spatial resolutions.

8.3.9 Parallel computational efficiency

Performance improvements are largely due to increased parallelism rather than improved microprocessor clock frequency. Hence the numerical algorithm should be amenable for execution on massively parallel computing platforms. A way to achieve this is to use local methods with minimal global dependence (for more discussion see chapter 16).

It is worth noting that although computing power has increased dramatically in the last 20 years or so, these extra computational resources have largely been used to satisfy demands for higher resolution, more advanced physical parameterizations and coupling the atmospheric component to ocean, land, and ice components (i.e. coupled models). Hence it is still desirable to develop efficient dynamical core algorithms, in particular, schemes for efficient tracer transport (see paragraph on *Multi-tracer efficiency* below) even though computing power is increasing.

8.3.10 Multi-tracer efficiency

In modern atmospheric models the number of tracers required to be advected continue to increase. For example, the chemistry version of NCAR's CAM model transports over 100 tracers (Lamarque et al, 2008). Given that the dynamical core typically has less than 10 prognostic variables defining the state of the fluid flow and thermodynamics, the computational cost of running the dynamical core can primarily be attributed to the transport of tracers. Needless to say, it is highly desirable that the numerical algorithm used for tracer transport be efficient and adaptable for a large number of tracers. A way to achieve multi-tracer efficiency is to design schemes that can reuse information for each additional tracer (Barth and Frederickson, 1990; Dukowicz and Baumgardner, 2000) and/or transport tracers with longer time-steps than used for the continuity equation for air in the dynamical core (also referred to as 'super-cycling' of tracers with respect to air or, more commonly, 'sub-cycling' of air with respect to tracers; see section 8.7.2).

8.3.11 Geometric flexibility

It is generally useful to develop numerical methods that can be used on a wide range of spherical grids. Next generation dynamical cores are being developed on spherical grids based on triangles, quadrilateral, pentagonal and/or hexagonal control volumes. It is therefore desirable that a scheme can handle any spherical polygon-based grid. Also models using static or adaptive mesh-refinement benefit from geometrically flexible methods. An example of a geometrically flexible advection scheme is MPDATA (Multidimensional Positive Definite Advection Transport Algorithm); for an overview see Smolarkiewicz (2006).

8.4 Problem formulation: Discrete schemes

Finite-volume methods are numerical methods where each prognostic variable is stored as an average quantity over a certain finitely large control volume (also

referred to as cell-integrated methods). This choice differs from methods that are based on grid-point values (used in, e.g., finite-difference methods) or weights for expansion functions (e.g., finite-element or spectral method). In order to derive finite-volume discretization schemes the equations of motion, in this case the continuity equation, are integrated over a control volume. This allows for discretizations that keep track exactly of the local mass-budgets and thus provides mass-conservation to machine precision. Note that although finite-volume schemes are designed to conserve mass locally through explicitly tracking mass, conservation of mass can also be achieved in non finite-volume methods (e.g., compatible methods, see chapter 12). Conservative methods that are not finite-volume methods usually do not conserve mass locally.

Typically finite-volume schemes come in two flavors corresponding to two forms of deriving the equations of motion from first principles: Eulerian and Lagrangian [13]. In most textbooks the equations of motion are derived in Eulerian form, that is, as observed from a fixed volume in the atmosphere (stationary to the Earth's surface). Hence there is a flux of mass through the volume boundaries unless the local wind is zero. One may also derive the equations of motion as viewed by a volume not just rotating with the Earth's rotation axis but also moving with the local flow; a.k.a. Lagrangian form. In Lagrangian form there is no flux of mass through the 'walls' of the volume. Both of these forms of the finite-volume discretization of the continuity equation are presented next after the introduction of some notation. For simplicity we consider the two-dimensional problem in Cartesian geometry and defer the discussion of the extension to spherical geometry and three-dimensions to section 8.5.3.3 and 8.6, respectively.

Let the domain of integration be denoted Ω (a Cartesian plane with periodic boundary conditions or no flux through the domain boundaries). The domain Ω is partitioned into N non-overlapping grid cells, A_k, $k = 1,..,N$, so that $\bigcup_{k=1}^{N} A_k$ span Ω. The area of cell A_k is denoted ΔA_k. For now we shall assume a quadrilateral mesh in Cartesian geometry, however, the discussion can trivially be extended to other meshes such as triangular or hexagonal meshes in Cartesian geometry.

As mentioned above the prognostic variable considered is the cell averaged value

$$\overline{\psi}_k = \frac{1}{\Delta A_k} \int_{A_k} \psi(x,y)\, dA, \quad \psi = \rho \text{ or } \rho q, \tag{8.18}$$

where $\psi(x,y)$ is the exact solution. In time we discretize in terms at equidistant time-levels, i.e. superscript n refers to the quantity at time $t = n\Delta t$ where Δt is the time-step. So the state of a tracer in cell A_k at time-level n is denoted $\overline{\psi}_k^n$.

[13] the Eulerian and Lagrangian forms are limits of the more general arbitrary Lagrangian-Eulerian (ALE) form (Hirt et al, 1974)

8.4.1 (Semi-)Lagrangian schemes

Consider an arbitrary Lagrangian area $A(t)$. By definition the area $A(t)$ moves with the flow without any flux of mass through its sides and hence it always contains the same material particles. Since there is no flux of mass through the boundaries of $A(t)$, the mass in the area is conserved. In mathematical terms this can be written as

$$\frac{d}{dt}\int_{A(t)} \psi \, dA = 0, \quad \psi = \rho \text{ or } \rho q. \tag{8.19}$$

Equation (8.19) is referred to as the Lagrangian finite-volume form of the continuity equation. A temporal discretization of (8.19) reads

$$\int_{A(t+\Delta t)} \psi \, dA = \int_{A(t)} \psi \, dA. \tag{8.20}$$

If the same Lagrangian cell $A(t)$ is tracked throughout the simulation the resulting scheme is referred to as fully Lagrangian. The challenge in such schemes is that for non-trivial flows the areas quickly deform into thin filaments so that the resolution is no longer uniform (see Figure 2 in chapter 7).

Instead one may consider a different set of areas/parcels at every time-step, for example, enforcing that either $A(t+\Delta t)$ or $A(t)$ is a regular static grid cell. Such an approach is referred to as semi-Lagrangian since it only tracks the same Lagrangian parcels/area for one time-step. The advantage of the semi-Lagrangian approach, as compared to a fully Lagrangian method, is that it retains a quasi uniform resolution as the mesh only deforms for one time-step. However, the grid uniformity is introduced at the expense of having to interpolate variables from a regular static grid to a deformed Lagrangian grid (or vice versa) at every time-step. How this interpolation can be done is discussed in great detail below but for now more mathematical notation is needed.

Assume that $A(t+\Delta t)$ is a regular grid cell resulting in a method referred as upstream semi-Lagrangian[14]. If we consider cell k in the discretized domain then the regular grid cell $(A(t+\Delta t))$ is exactly A_k with area ΔA_k. The corresponding upstream Lagrangian area $(A(t))$ is referred to as a_k with area Δa_k (see Fig. 8.6a). We assume that Δ is chosen such that all the deformed areas a_k are simply connected.

Note that there exists a one-to-one correspondence between A_k and a_k such that the a_k's span Ω without gaps or overlaps between them

$$\bigcup_{k=1}^{N} a_k = \Omega, \text{ and } a_k \cap a_\ell = \emptyset \, \forall k \neq \ell. \tag{8.21}$$

Assume that the evolution of the Lagrangian grid is known analytically so we know the characteristics or trajectories for each fluid parcel at all times. The computation

[14] note that one might equally well consider downstream schemes where one considers Eulerian (regular) grid cells at time-level n and let them be transported with the flow for one time-step.

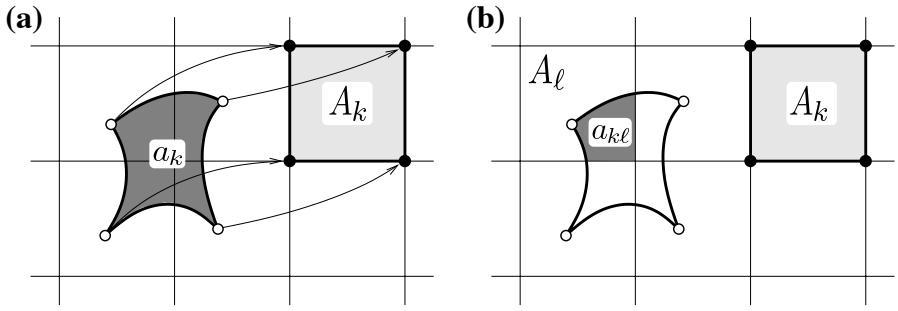

Fig. 8.6 A graphical illustration of the upstream semi-Lagrangian nomenclature. (a) The static Eulerian cell A_k (light shading) and the corresponding upstream Lagrangian area a_k (dark shading) that ends up at A_k after one time-step. For illustration the trajectories of the vertices (filled circles) of A_k are depicted with arrows. The corresponding upstream vertices (departure points) are shown with open circles. (b) The notation used to define overlap areas between Eulerian cell A_ℓ and upstream Lagrangian area a_k is $a_{k\ell} = A_\ell \cap a_k$ (dark shaded area)

of fluid parcel trajectories is well developed in the semi-Lagrangian literature (e.g., Staniforth and Côté 1991, Staniforth et al 2003, Hortal 2002) and in the interest of brevity it is not discussed further in this chapter, although accurate trajectories are vital for the accuracy of any Lagrangian method.

With the notation introduced above the forecast equation (8.20) can be written as

$$\overline{\psi}_k^{n+1} \Delta A_k = \overline{\psi}_k^n \Delta a_k. \tag{8.22}$$

where $\overline{\psi}_k^n$ is the average tracer density over the upstream area a_k

$$\overline{\psi}_k^n = \frac{1}{\Delta a_k} \int_{a_k} \psi^n(x,y)\, dA, \tag{8.23}$$

and $\overline{\psi}_k^{n+1}$ is the cell averaged value of ψ over the regular area A_k at time-level $n+1$. The function $\psi^n(x,y)$ is the continuous distribution of ψ at time-level n. Obviously, since the prognostic variables are cell averages $\overline{\psi}$ we do not know the variation of ψ at the sub-grid scale and $\psi^n(x,y)$ must be reconstructed from the prognostic cell averages[15]. This procedure is referred to as sub-grid-scale reconstruction. In finite-volume schemes the reconstruction is usually local rather than global. So each cell k will have an associated sub-grid-scale reconstruction function $\psi_k(x,y)$ rather than one global reconstruction function over all cells such as the spherical harmonic functions used in spectral transform models.

Hence the global reconstruction function is a collection of local reconstruction functions

$$\psi(x,y) = \sum_{k=1}^{N} I_{A_k} \psi_k(x,y), \tag{8.24}$$

[15] unless variables such as gradients are also carried as prognostic variables (e.g. Yabe et al, 2001)

where I_{A_k} is the indicator function

$$I_{A_k} = \begin{cases} 1, (x,y) \in A_k, \\ \\ 0, (x,y) \notin A_k. \end{cases} \tag{8.25}$$

Commonly used methods for computing $\psi_k(x,y)$ from $\overline{\psi}_k$ are discussed in section 8.5.2.

First, we note that $\psi(x,y)$ is not necessary continuous or differentiable across cell boundaries. So if the upstream area a_k covers several Eulerian cells (e.g., Fig. 8.6), the integral on the right-hand side of (8.23) must be broken up into overlap areas between Eulerian cells and a_k. The discretized semi-Lagrangian finite-volume continuity equation (8.22) then reads

$$\overline{\psi}_k^{n+1} \Delta A_k = \sum_{\ell=1}^{L_k} \int_{a_{k\ell}} \psi_\ell^n(x,y)\, dA. \tag{8.26}$$

The number of non-empty overlap areas between the upstream cell (departure cell) a_k and the Eulerian grid cells is denoted L_k. Note that L_k depends on the flow and time-step size, and for time-varying flows it is not necessarily constant. The area $a_{k\ell}$ is the non-empty overlap area between the upstream cell a_k and the Eulerian grid cell A_ℓ (see Fig. 8.6b)

$$a_{k\ell} = a_k \cap A_\ell, \quad a_{k\ell} \neq \emptyset; \quad \ell = 1, \ldots, L_k, \text{ and } 1 \leq L_k \leq N, \tag{8.27}$$

where N is the number of cells in the domain.

Two conditions must be fulfilled to get conservation of mass in Lagrangian finite-volume schemes: Firstly, the upstream cells a_k must be simply connected domains and they must span Ω without gaps or overlaps (equation 8.21). Secondly, the reconstruction function in cell k, $\psi_k(x,y)$, must be conservative in the sense that the integral of $\psi_k(x,y)$ over A_k must yield the cell-average value that is used as prognostic variable,

$$\frac{1}{\Delta A_k} \int_{A_k} \psi_k(x,y)\, dA = \overline{\psi}_k. \tag{8.28}$$

Equation (8.26) is the basic finite-volume form of the continuity equation when using an upstream finite-volume semi-Lagrangian approach. Obviously we do not know the exact Lagrangian trajectory of every parcel in the domain so some approximation to a_k is necessary for the derivation of any practical scheme. This is discussed in section 8.5.1.

In the discussion above ψ generically refers to both ρ and ρq. In the reconstruction of ρq one may chose to reconstruct ρ and q separately and combine them to provide a reconstruction for the product ρq. There are several reasons for choosing this approach. First, it is q and not ρq that is conserved along parcel trajectories (see equation 8.11) and q should therefore obey monotonicity requirements. Hence one can argue that monotone reconstruction function filters (discussed in section 8.5.2)

should be applied to q and not ρq. Second, the consistent coupling of tracers and air density equations in cell-integrated semi-Lagrangian schemes as well as ensuring monotone forecasts of q, is perhaps easier when choosing this approach (Nair and Lauritzen, 2010).

The reconstructions for ρ and q can be combined to provide a reconstruction for ρq by simply multiplying the reconstruction functions for ρ and q as done in Dukowicz and Baumgardner (2000). However, in doing so mass-correction terms may be needed to satisfy (8.28) for higher-order reconstructions. The downside of this approach is that if, for example, the reconstruction function for ρ and q are polynomials of ith and jth order the product will be polynomials of $(i+j)$th order which may be computationally intensive to integrate. One may simplify by removing some terms from the product as done in Nair and Lauritzen (2010). The latter also facilitates rendering schemes monotone in q. In Eulerian schemes, discussed next, tracer mixing ratio and air density are usually reconstructed separately for sub-cycling (see section 8.7.2)

8.4.2 Eulerian scheme

Contrary to the Lagrangian derivations in the previous section, the equations of motion are typically derived in Eulerian form. In the context of the finite-volume form of the continuity equation the Eulerian approach keeps track of the flux of mass through the Eulerian cell walls rather than tracking the mass in a cell moving with the flow. A more formal derivation is given below.

First, integrate (8.9) or (8.10) in space over a grid cell A_k

$$\int_{A_k} \frac{\partial \psi}{\partial t}\, dA + \int_{A_k} \nabla \cdot (\psi \mathbf{v})\, dA = 0, \text{ where } \psi = \rho, \rho q. \tag{8.29}$$

On integrating the first term on the left-hand side of (8.29) to get the area average and applying the divergence theorem to the second term we get

$$\frac{d}{dt}\left(\overline{\psi}_k \Delta A_k\right) + \oint_{\partial A_k} (\psi \mathbf{v}) \cdot \mathbf{n}\, dS = 0, \tag{8.30}$$

where ∂A_k is the boundary of A_k and $\mathbf{n}$ the outward normal vector to ∂A_k. The second-term on the left-hand side of (8.29) represents the instantaneous flux of mass through the boundaries of A_k. Temporal integration of (8.30) over one time-step yields

$$\overline{\psi}_k^{n+1} \Delta A_k = \overline{\psi}_k^{n} \Delta A_k - \int_{n\Delta t}^{(n+1)\Delta t} \left[\oint_{\partial A_k} (\psi \mathbf{v}) \cdot \mathbf{n}\, dS \right] dt, \tag{8.31}$$

after re-arranging terms. The second term on the right-hand side of (8.31) is the flux of mass through the walls of A_k during one time-step. A graphical illustration of the fluxes is given in Figure 8.7 and discussed in the next paragraph.

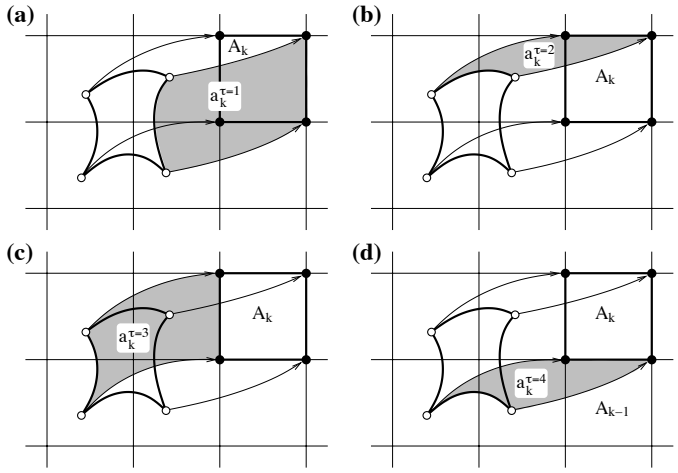

Fig. 8.7 A graphical illustration of the 'flux-areas' associated with Eulerian cell A_k (area in the upper right corner of each plot bounded by thick lines). For each vertex of cell A_k (filled circles) the upstream trajectories are shown (curved arrows departing from open circles). The shaded areas show the flux-areas for the (a) east $a_k^{\tau=1}$, (b) north $a_k^{\tau=2}$, (c) west $a_k^{\tau=3}$ and (d) south $a_k^{\tau=4}$ face, respectively, using standard compass orientation. These areas are swept through each face during one time-step. See text for details.

Let τ denote the face number and N^f the number of faces of the cells. For simplicity we assume a quadrilateral mesh $N^f = 4$, however, the method can accommodate any kind of mesh (for example, for a triangular and hexagonal mesh N^f would be 3 and 6, respectively). A graphical illustration of the fluxes through the cell walls for Eulerian cell k are shown on Fig. 8.7. As will become clear, the Figure also shows the upstream Lagrangian cell although it is not explicitly needed for flux computations. The sides of the Eulerian control volume are numbered counter-clockwise so that sides $\tau = 1,2,3,4$ correspond to the east, north, west and south walls, respectively (using standard compass notation). The flux of mass through the side $\tau = 1$ corresponds to the mass over the shaded area on Fig. 8.7a that is 'swept' through the wall during one time step. The shaded area, referred to as $a_k^{\tau=1}$, is bounded by the face $\tau = 1$, the two upstream trajectories for the end points of face $\tau = 1$, and the upstream translation of the side $\tau = 1$. We will refer to $a_k^{\tau=1}$ as the 'flux-area' for face $\tau = 1$. Similarly, the fluxes through the remaining cell sides are illustrated in Fig. 8.7b-d.

Using the notation introduced above (8.31) can be written as

$$\overline{\psi}_k^{n+1} \Delta A_k = \overline{\psi}_k^n \Delta A_k - \sum_{\tau=1}^{N^f} F_k^\tau, \tag{8.32}$$

where F_k^τ is the flux of mass through face τ during one time-step

$$F_k^\tau = s_k^\tau \int_{a_k^\tau} \psi^n(x,y)\, dA. \tag{8.33}$$

The 'flow-direction' function s_k^τ is used to indicate inflow and outflow

$$s_k^\tau = \mathrm{sgn}(\mathbf{v}\cdot\mathbf{n}), \tag{8.34}$$

where $\mathrm{sgn}(\cdot)$ is the sign-function. Hence s_k^τ is 1 for outflow and -1 for inflow[16]. In Figure 8.7 the flow-direction function s_k^τ is 1 for $\tau = 1,2$ and -1 for $\tau = 3,4$.

Note that the flux of mass through one cell wall is identical, but with opposite sign, to the flux of mass through the neighboring cell that it shares a face with. For the example on Figure 8.7d

$$a_k^{\tau=4} = a_{k-1}^{\tau=2}, \tag{8.35}$$

where the cell located immediately to the south of the Eulerian cell A_k is A_{k-1}. So in a practical implementation of a scheme based on (8.32) only two fluxes per cell are computed if $N^f = 4$.

Although the scheme outlined above is termed 'Eulerian' it is not Eulerian in the classical sense where the space and time dimensions are separated. In other words, the scheme outlined above could also be termed flux-form semi-Lagrangian since flux-areas that move with the flow are tracked ('remap-type' scheme). It is Eulerian in the sense that we consider the flux of mass through the (stationary or Eulerian) cell walls. When separating the temporal and spatial dimensions, as done in classical Eulerian schemes, there are no trajectory calculations and fluxes are computed using local information and partial derivatives along the coordinate directions at specific times. The temporal discretization is usually based on Runga-Kutta methods (see chapter 6). One may argue that the classical Eulerian schemes are an approximation of the general Eulerian-Lagrangian concept presented in this chapter where true (along the trajectories) fluxes are approximated with partial fluxes (i.e., the particle path vector can be decomposed into vector components along the coordinate axes).

8.4.3 Equivalence between the Lagrangian and Eulerian discretizations

It is interesting to note the equivalence between the Lagrangian finite-volume continuity equation (8.26) and the Eulerian version (8.32): If taking the sum of the flux-areas a_k^τ with weight 1 for outflow and weight -1 for inflow as well as A_k with weight 1 (all areas involved on the right-hand side of (8.32)), the upstream Lagrangian area a_k results (see example on Fig. 8.7). That is, the right-hand side of (8.32) written in terms of areas is

[16] for simplicity we do not consider the situation where s_k^τ is multi-valued along a particular face. For more details on such a situation see Harris et al (2010)

$$\Delta A_k - \sum_{\tau=1}^{N^f} (s_k^\tau \Delta a_k^\tau) = \Delta a_k. \tag{8.36}$$

So the Lagrangian and Eulerian schemes are identical, as expected, since no approximations have been made so far (even if approximations are made and the resulting schemes are applied to the Euler equations, Eulerian and semi-Lagrangian schemes may produce very similar results as shown in Leslie and Dietachmayer, 1997). Insights into schemes can be obtained in the light of the equivalence described above. Any Eulerian flux-form scheme should ideally and effectively have an associated upstream cell from which information is fetched (a.k.a. domain of dependence) to produce the forecast. A more detailed discussion is given in section 8.5.1.2.

A significant difference between the Lagrangian and Eulerian formulation is the necessary conditions for mass conservation. Given a mass-conservative reconstruction function (8.28), a necessary condition for the Lagrangian scheme to be conservative is that the upstream areas a_k span the domain Ω without overlap and gaps between them (8.21) and that the reconstruction function is mass-conservative (8.23). For the Eulerian scheme, however, the flux-areas a_k^τ need not necessarily to span the domain Ω and the reconstruction function does not need to satisfy (8.23) to produce a mass-conservative scheme. In fact any estimation of the flux will provide an inherently mass-conservative scheme since the flux computed for a particular cell wall is subtracted in the neighboring cell with which it shares that particular face. So the Lagrangian scheme has, in the sense described above, a stricter requirement for mass-conservation than the Eulerian flux-form formulation.

Another significant difference between the Eulerian and Lagrangian formulations is that the Lagrangian formulation requires the upstream areas to be simply-connected domains. The Eulerian formulation does not require that, in fact, even for relatively simple flows the flux-areas can be non-simply connected (see, e.g., Fig.2 in Harris et al 2010). The Eulerian formulation is therefore more robust in the sense that it can handle non-simply connected flux-areas (and conserve mass simultaneously) whereas the Lagrangian scheme will break down if an upstream area is not simply connected. This difference could be important for an operational application of the scheme.

8.5 Discrete schemes: Approximations

The Lagrangian and Eulerian finite-volume schemes, given in (8.26) and (8.32) respectively, are exact. Hence we assume the trajectory of every parcel is known exactly (the exact upstream area and flux-areas are known), the sub-grid-cell reconstruction is exact and the integration of the sub-grid-cell reconstruction function over the upstream areas and flux-areas can be done analytically. Now we start to discuss some of the approximations that can be made in order to derive practical numerical schemes that only have a finite number of degrees of freedom. The approximations can be divided into four steps: Computation of parcel trajectories, area

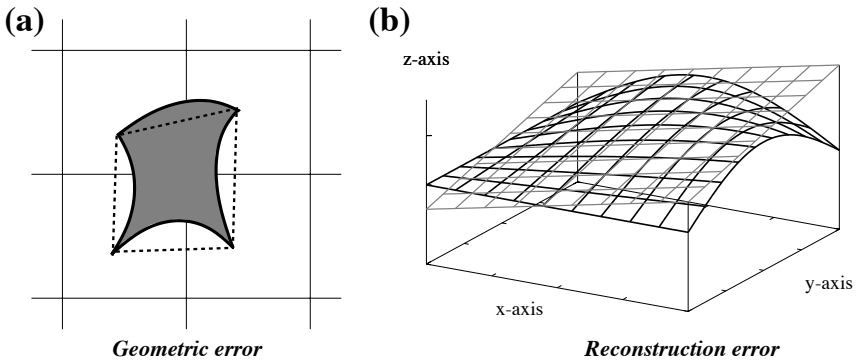

Fig. 8.8 A schematic illustration of the (a) geometric error and (b) reconstruction (gradient) error, respectively, for a cell in two dimensions. (a) The geometric error occurs due to the exact region of integration (shaded area) being approximated by, for example, straight line segments (dashed lines). (b) The reconstruction error refers to the numerical methods inability to reconstruct the exact sub-grid-scale variation (black line surface). The grey lines contour the reconstructed sub-grid-scale distribution (in this case a linear approximation).

approximation (either upstream Lagrangian areas or Eulerian flux-areas), sub-grid-cell reconstruction and integration of $\psi^n(x,y)$ over deformed areas. As already mentioned we will not discuss the computation of trajectories here and therefore simply assume that they are given.

Firstly, the approximation to areas are discussed. Once the areas have been defined, the transport problem has been reduced to a remapping problem, that is, a conservative grid-to-grid interpolation problem. This requires a reconstruction of the sub-grid-cell distribution and an integration over overlap areas. These three steps (area approximation, reconstruction, integration over overlap areas) are discussed separately below.

8.5.1 Approximation to areas

With only a finite-number of degrees of freedom and therefore only having the capability of tracking a finite number of parcels (typically the same number as cells N) some approximation must be made to the exact upstream Lagrangian area or Eulerian flux-area. The inability of the scheme to approximate the exact areas is referred to as the *geometric error* (Lauritzen and Nair, 2008) and is illustrated graphically on Fig. 8.8a. Obviously the geometric error may lead to local mass errors. Another error is due to inexact sub-grid-cell reconstruction. This error, referred to as the *reconstruction error*, is illustrated on Fig. 8.8b and discussed further in section 8.5.2. Strategies for area approximations are the subject of this section.

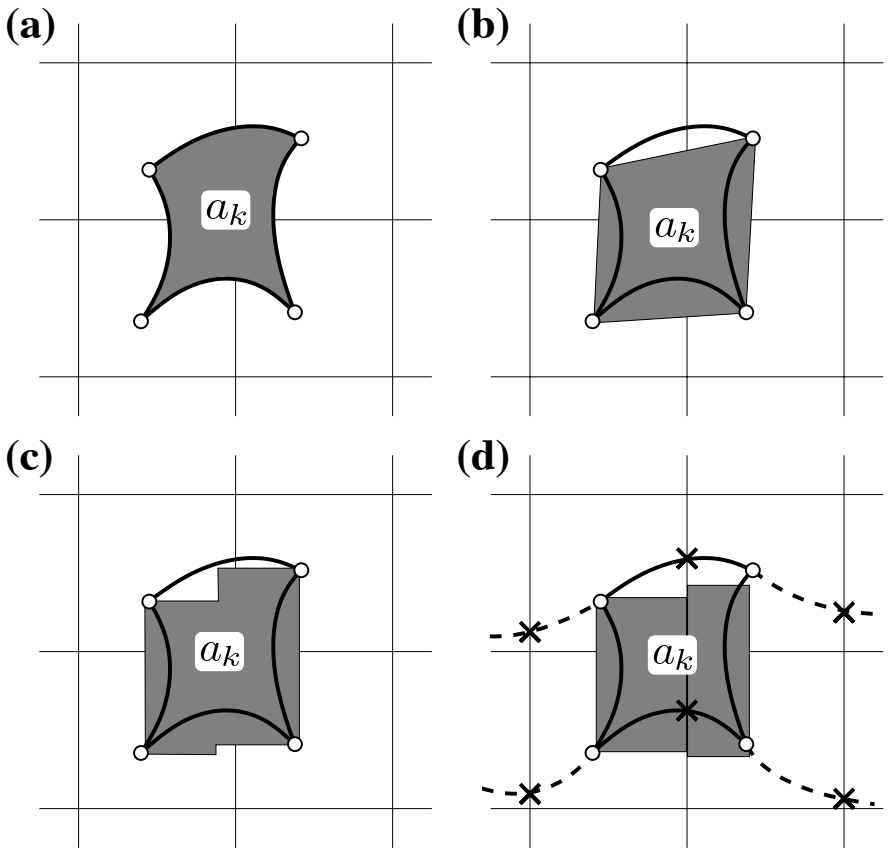

Fig. 8.9 Graphical illustration of approximations to the upstream Lagrangian cell a_k a.k.a. the departure cell. Assume the departure points corresponding to the vertices of the Eulerian grid cell are known (open circles). (a) Exact departure cell (shaded area) with sides depicted with thick lines. (b) Sides of the departure cell approximated with straight lines by connecting the departure points. (c) Departure cell approximation used in Nair and Machenhauer (2002) where the east and west sides are straight lines parallel to the Eulerian longitudes (y-axis on the plot) and the north and south sides are approximated with 'step functions'. (d) The Lagrangian cell used in the cascade schemes that are based on intersections (crosses) between the Lagrangian latitudes (dashed/solid curved lines) and the Eulerian longitudes. The 'step' in the step functions used in the cascade schemes always coincides with the Eulerian longitudes (x-isolines on the Figure).

8.5.1.1 Lagrangian area approximations

Fully two-dimensional Lagrangian area approximations

Probably the most rigorous approximation to the exact upstream cell a_k, Figure 8.9a, is to follow the trajectories of the vertices of A_k upstream and then connect the upstream vertices with straight lines (Fig. 8.9b); (Rančić 1992, Lauritzen et al 2010).

All other approximations involve approximating a_k with line segments parallel to the coordinates axis which, in general, simplifies the overlap-area integration algorithm. Some examples are given on Fig. 8.9. For more details on Lagrangian cell approximations for orthogonal meshes see the comprehensive review by Lauritzen et al (2006) and Machenhauer et al (2009).

Flow-split Lagrangian area approximations

More recently the finite-volume cascade[17] approach was suggested by Nair et al (2002) and Zerroukat et al (2002) which uses a combination of Eulerian and Lagrangian operators, that is, the one-dimensional operators are successively applied along a coordinate line and a Lagrangian line, respectively. An example is given in Fig. 8.9d where the first one-dimensional operator is applied along the Eulerian longitudinal direction and the second is applied along the deformed Lagrangian latitude (curved solid/dash lines on Figure 8.9d). So rather than being a fixed direction based splitting method it is flow-based (for a review see Machenhauer et al 2009). The upstream Lagrangian cell for the cascade scheme is illustrated on Figure 8.9d. The main difference between the fully two-dimensional area approximation used in Nair and Machenhauer (2002), shown on Figure 8.9c, and the cascade scheme area approximation, is the location of the 'jump' in the north and south sides of the departure cell. Since the first cascade 'sweep' is along Eulerian longitudes the jump in the north and south sides coincide with an Eulerian longitude. In the Nair and Machenhauer (2002) the jump is located midway between the east and west cell sides.

Approximating the Lagrangian cell with line-segments parallel to the coordinate axis, either with fully two-dimensional or cascade methods, is attractive for orthogonal grids such as a Cartesian rectangular mesh (e.g., Zerroukat et al 2002) and a regular latitude-longitude grid on the sphere (e.g., Nair and Machenhauer 2002, Nair et al 2002, Zerroukat et al 2004). It is less obvious how to extend such approaches to non-orthogonal grids such as triangular or hexagonal grids since the cell sides are no longer orthogonal.

8.5.1.2 Eulerian flux area approximations

The approximation to flux-areas in Eulerian schemes can be divided into two categories: Fully two-dimensional approximations to the flux-areas and dimensionally split area approximations. We remind the reader that only methods that have been extended to global spherical domains are discussed here. We are thereby excluding many transport schemes published in the meteorological literature.

[17] the non-conservative cascade interpolation method in Cartesian geometry was introduced by Purser and Leslie (1991)

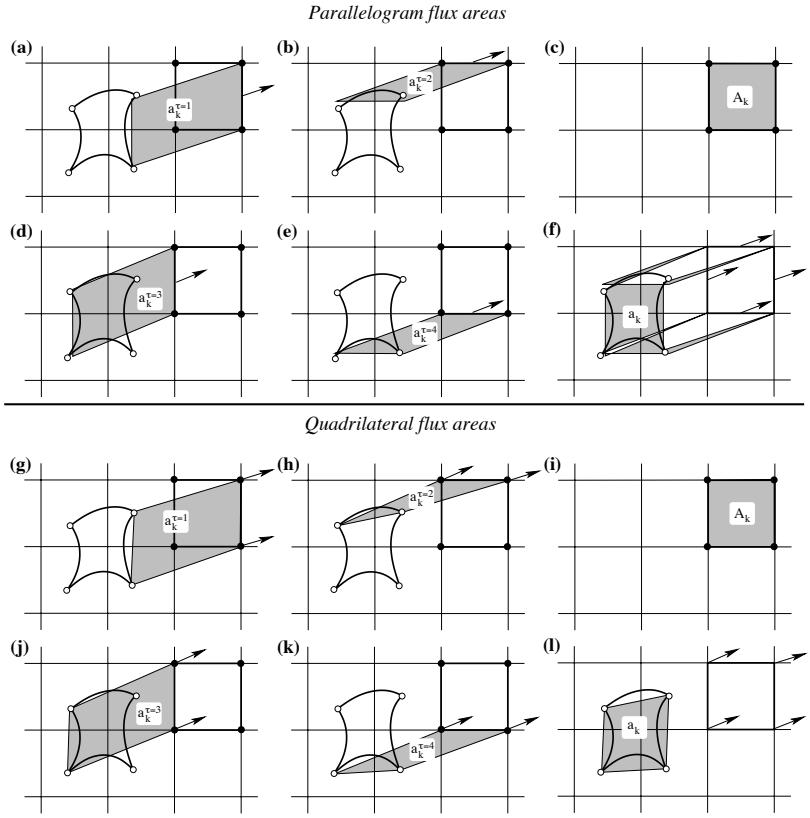

Fig. 8.10 A schematic illustration of different flux approximations, parallelogram (a,b,d,e) and quadrilateral (g,h,j,k) flux-areas, and the equivalent upstream Lagrangian areas (f,l). The equivalent upstream areas are computed by taking the sum of all areas involved in the forecast (a,b,c,d,e) or (g,h,i,j,k) with appropriate signs (see equation (8.36)). The velocity vectors used for the flux computations are also shown. The exact upstream Lagrangian cell (open circles connected with curved lines) is also shown although it is not explicitly used in the flux-form schemes.

Fully two-dimensional flux-area approximations

The fully two-dimensional flux-area approximations can be divided into two categories. Firstly, one in which one face-centered velocity vector per face is used to trace back the flux-area and, secondly, the approach in which the vertices of the face are traced upstream to compute the flux-area. The first approach only has one degree of freedom for the flux-areas whereas the latter approach has two. Consequently the resulting flux-areas are parallelograms and arbitrary quadrilaterals, respectively, for the two approaches. An elaboration is given below.

Recently, Miura (2007) suggested to approximate the flux-areas from a face-centered wind velocity. So the two vertices of the face would have identical up-

stream displacements based on the same face-centered velocity vector. The trajectories are therefore parallel and have the exact same length. Hence the flux-areas a_k^τ, $\tau = 1,2,3,4$, are parallelograms (Fig. 8.10a,b,d,e, respectively). The fact that the upstream area is a parallelogram may simplify the practical integration of overlap areas at the expense of some potential loss of accuracy if the flow is highly deformational. This is illustrated by computing the effective upstream Lagrangian area for the Miura (2007) scheme using the method outlined in section 8.4.3. That is, by taking the sum of the flux-areas (with signs) shown on Figure 8.10a,b,d,e and the Eulerian area (Fig. 8.10c), the effective upstream area a_k results (Figure 8.10f). The upstream area mostly coincides with the exact departure cell, however, there are minor contributions tracing the Eulerian cell vertices that are non-local (not overlapping with the true departure cell). Also, the flux-areas for all cells do not span the domain Ω. If the flow is constant (no deformation) the non-local part of the flux-areas disappear as all the face-centered velocity vectors would be aligned.

If this inability of representing the local flux-areas (geometric error) is a significant source of error has not been investigated (as far as the authors are aware) and the error would only show for challenging test cases with strong deformation. For example, the widely used solid body advection test on the sphere would most likely not expose this potential deficiency. An illustrative example of a highly deformational flow is given on Figure 8.11 that shows the Lagrangian (upstream) grid for each cubed-sphere panel for one of the test cases in Nair and Lauritzen (2010). Even for a relative short time-step (resulting in a maximum CFL number in each coordinate direction of approximately 0.8) the upstream cells are highly deformed and they might be challenging to approximate accurately using simplified fluxes unless very short time-steps are used. It should, however, be noted that the geometric discussed above will only show if it is larger than the reconstruction error. Consquently, the geometric error is most likely not significant when using low-order reconstruction functions (constant or linear reconstructions).

The potential non-locality problem described above can be resolved by instead of using one face-centered vector (for the trajectories) per face, to use trajectories for the vertices of the cell A_k (Rančić, 1992; Lipscomb and Ringler, 2005; Yeh, 2007). This extra degree of freedom allows the flux-areas to deform into arbitrary quadrilaterals. The equivalent upstream area now equals the Lagrangian area resulting from connecting the upstream points with straight lines. This can be shown as above by taking the sum of the areas involved in the forecast equation (8.32), Fig. 8.10g,h,j,k,i, with appropriate weights (signs). As for the Eulerian-Lagrangian equivalence in the continuous case, discussed in section 8.4.3, this approximate flux-form scheme is exactly equivalent to the approximate Lagrangian scheme discussed above where the departure points are connected with straight lines (Fig. 8.10l and Fig. 8.9b, respectively).

Improving the effective approximation to the upstream area further would involve the introduction of more parcels that are tracked (as suggested by Lauritzen et al 2010) or some approximation to the sides with curved lines. A cursory study addressing the potential benefits of approximating the upstream areas with higher-

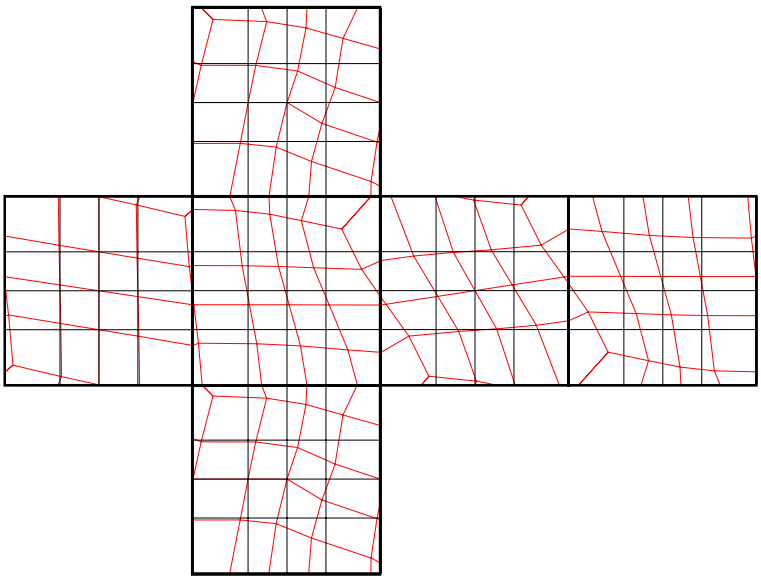

Fig. 8.11 The static Eulerian grid (thin lines aligned with coordinate lines) and departure grid (deformed thin lines) at the first time-step shown on the gnomonic projection on each cubed-sphere panel for test case 1 of Nair and Lauritzen (2010) illustrated on Fig. 8.3 (time-step was chosen such that the maximum CFL number is approximately 0.8). The departure grid has been constructed by computing trajectories for the cell vertices and then the vertices are connected with straight lines (great-circle arcs on the sphere).

order polygons was performed in Harris et al (2010) within the context of a flux-form semi-Lagrangian scheme.

Dimensionally split flux-areas

A popular approach not discussed so far is to use a sequence of one-dimensional operators to approximate the two-dimensional fluxes thereby eliminating the need for solving a fully two-dimensional remapping problem. These methods are also referred to as dimensionally split approaches. A popular scheme based on this strategy is presented in Lin and Rood (1996) and Leonard et al (1996).

In the present discussion on effective upstream areas, this operator splitting approach was analyzed by Lauritzen (2007) and Machenhauer et al (2009). When using dimensionally split approaches the effective upstream area is approximated with a combination of rectangles aligned with the grid lines and with different weights (see Machenhauer et al 2009). One-dimensional operators cannot represent areas skew to the face in question. As an example of an operator splitting approach the effective departure area for the Lin and Rood (1996) scheme is given on Fig. 8.12 for

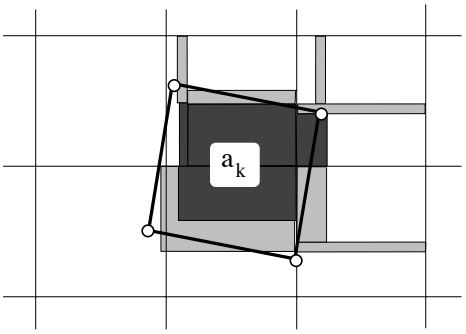

Fig. 8.12 A graphical illustration of the effective departure area a_k for the Lin and Rood (1996) scheme using an analytic wind field which is deformational, rotational and divergent. The exact departure cell is shown with thick black lines (and open circles as vertices). Light shading shows the parts of the departure area where mass is weighted with 1/2 and dark shaded areas are weighted with 1. See Machenhauer et al (2009) for details.

a flow that has a translational, deformation and rotational component (see Machenhauer et al 2009 for details).

In dimensional split schemes one can obtain preservation of a constant density field in a non-divergent flow field. This property is harder to obtain with fully two-dimensional semi-Lagrangian schemes but it is possible with cascade semi-Lagrangian schemes (Thuburn et al, 2010).

8.5.1.3 Comment on area approximations

One might argue that the errors associated with some of the simplified flux- and upstream- area approximations are not significant at least for orthogonal meshes. For example, for semi-Lagrangian finite-volume schemes Lauritzen et al (2010) found little difference between the rigorous upstream area approximation and simpler area approximations using line-segments parallel to the coordinate axis.

On non-traditional meshes simplified fluxes might introduce significant inaccuracies. For example, considering a solid-body rotation flow field on the sphere on a non-traditional grid such as the cubed-sphere grid, some of the Lagrangian areas are highly deformed even though the flow field is non-divergent, non-deformational and non-rotational. This is illustrated on Fig. 8.13. The Lagrangian cells entering a cubed-sphere panel from neighboring panels are highly skewed compared to the Lagrangian areas staying within the panel in question. Therefore the need for fully two-dimensional area approximations for non-traditional grid applications seems more evident than for orthogonal quadrilateral grids such as the regular latitude-longitude grid. All of the above is, of course, assuming that the reconstruction error is smaller than the geometric error which will most likely not be the case for first- and second-order methods.

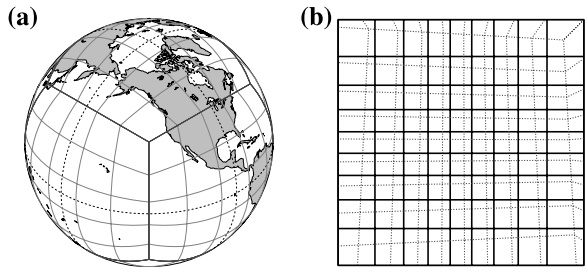

Fig. 8.13 (a) Cubed-sphere grid shown with light shaded lines and panel edges with black lines. (b) The upstream/departure grid (dashed lines) shown on a local (gnomonic) projection for one of the cubed-sphere panels using the solid-body advection flow field (time-step is so that one revolution is completed in 72 time-steps. The solid lines show the Eulerian static grid. The skewed departure cells are cells entering from neighboring panels during the time-step. The parts of the departure cells outside the panel have been 'chopped off'. For an introduction to the cubed-sphere grid see, e.g., chapter 9.

Velocity staggering and flux-areas

For the different flux-area approximations described above the velocity components are needed at the center of cell faces (for parallelogram flux areas), cell vertices (for the quadrilateral flux areas) or at multiple locations along the cell sides (for higher-order polygon fluxes). To avoid any interpolation of velocity components Arakawa B and E grid staggering (see chapter 3) should be used for quadrilateral and parallelogram flux areas, respectively, whereas the higher-order polygon flux inevitably will require interpolation of the velocity components (at least at a subset of the points along the cell sides). The interpolation of velocity components can potentially degrade the overall accuracy of the scheme (McGregor, 2005) and the choice of variable staggering impacts wave propagation (when solving the air mass continuity equation with the momentum equations) as discussed in chapter 3. Hence the choice of flux-area approximation and variable staggering are 'intertwined' and the choices impact not only the accuracy of the transport operator but also wave propagation properties in full models as well as other properties such as the need for filtering etc. (see, e.g., chapter 13 and 14). A exhaustive discussion of optimal variable staggering and flux-area approximation is beyond the scope of this chapter.

8.5.2 Sub-grid-scale reconstruction

In the previous sections the geometrical approximation to the upstream areas and flux-areas have been discussed. Next comes the actual integration of $\psi(x,y)$ over these areas, for which a sub-grid-scale reconstruction of the tracer field is needed. We start by discussing reconstruction methods in one spatial dimension and then

briefly discuss two dimensional extensions before covering the integration of $\psi(x,y)$ over overlap areas.

8.5.2.1 One-dimensional reconstruction functions

The sub-grid-scale reconstruction is vital for the overall accuracy and efficiency of a scheme, and a thorough discussion is beyond the scope of this chapter. We will, however, discuss some of the most widely used methods. In principle any function could be used for reconstructions, however, the choice of reconstruction function has consequences for any finite-volume scheme. Here are some desirable properties for reconstruction functions that should be considered:

- *Locality*. Locality is generally desirable to maximize parallel efficiency; that is, the stencil (or halo) used for the reconstruction in any cell should use only a limited number of neighboring grid cells. The cells used in the reconstruction of a given cell are referred to as the stencil of that cell.
- *Integrability*. The reconstruction function must later be integrated over overlap areas and it is convenient to use functions that can be integrated exactly. If polynomials are used, polynomials of successively higher degree will lead to more computationally expensive schemes.
- *Conservation*. For Lagrangian finite-volume schemes mass-conservation of the final algorithm requires the reconstruction function to satisfy the so-called cell-averaged property; namely, integration of the reconstruction over the cell (8.28) yields the known cell-average (for each prognostic variable). This requirement is not strictly necessary for Eulerian flux-form schemes but, in general, leads to more accurate reconstructions (Skamarock 2009; personal communication).
- *Filterable*. A scheme can be rendered monotone in the reconstruction step by filtering the reconstruction function so that it is monotone. It may therefore be desirable to use reconstruction functions that are amiable for such filtering. One thing to consider, for example, is that higher-degree polynomial reconstructions are more difficult to filter, since the number of possible extrema increases with the degree of the polynomial. For flux-form Eulerian schemes one may also render the solution monotone *a posteriori* by adequately 'mixing' the (usually low-order) monotone flux with the (usually higher-order) non-monotone flux (Zalesak, 1979). In the literature the *a posteriori* filtering is often referred to as limiting. An excellent review on limiting is given in Durran (1999), and we make no effort to try and reproduce it here. Certain reconstructions can also be used that are inherently non-oscillatory by design, such as the class of (W)ENO schemes ((Weighted) Essentially Non-Oscillatory schemes), which generally do not require filtering or limiting.
- *Exactness*. A reconstruction algorithm is referred to as p-exact if it exactly reproduces a global polynomial of degree p (Barth and Frederickson, 1990). Generally speaking, strict exactness constraints will lead to an increase in accuracy of the reconstruction function.

Polynomial reconstruction functions, mentioned a couple of times above, are a popular choice in the literature and all properties discussed above can be conveniently dealt with using such a basis. Some work has been done on nonpolynomial-based reconstruction functions (e.g. Norman and Nair, 2008; Xiao et al, 2002), however, we will focus on the former here. A comparison of various reconstruction functions in the context of conservative cascade interpolation was tackled by Norman et al (2009).

Reconstruction problem formulation (one dimension)

The one-dimensional reconstruction problem for a finite-volume scheme utilizing a polynomial basis can be stated as follows: Given discrete cell-averaged values $\overline{\psi}_k$ over cells A_k (here A_k refers to a 1D cell), determine coefficients $c_k^{(i)}$, $i = 1, \ldots, p$, so that

$$\psi_k(x) = c_k^{(0)} + c_k^{(1)} x + c_k^{(2)} x^2 + \ldots + c_k^{(p)} x^p, \tag{8.37}$$

is an approximation to the underlying field ψ in cell A_k. As mentioned previously, it is desirable that the reconstruction satisfies the cell-averaged property,

$$\int_{A_k} \psi_k(x)\, dx = \overline{\psi}_k \Delta x_k, \tag{8.38}$$

where Δx_k is the width of cell A_k. In the context of semi-Lagrangian advection schemes, this property is also referred to as the mass-conservation property.

In the cell-integrated continuity equation (8.18) $\overline{\psi}$ refers to either cell-averaged air density ρ or tracer density ρq, however, in the context of reconstructions it can be desirable to reconstruction ρ and q separately (as mentioned in section 8.4.1). In particular when enforcing shape-preservation it may be convenient to apply the filters/limiters to q and not ρq (e.g. Nair and Lauritzen, 2010). Hence, for the discussion on reconstructions ψ can either refer to ρ, ρq or q.

The Piecewise Constant Method (PCoM)

Perhaps the simplest sub-grid-scale representation is the so-called piecewise constant method (PCoM), which simply uses

$$\psi_k(x) = \overline{\psi}_k. \tag{8.39}$$

This approach is attributed to Godunov (1959) and trivially satisfies (8.38), does not need a halo, and is also inherently monotone since it cannot lead to new extrema. This approach is also formally first-order accurate and highly diffusive when used with any scheme over smooth flows and distributions. As a consequence, this choice of reconstruction is considered too diffusive for atmospheric transport prob-

lems (unless the flow is 'rough'), and so we must turn our attention to higher-order reconstructions.

Higher-order reconstructions

Note that by appropriately shifting the polynomial (8.37), we can always map A_k onto the normalized interval $x \in [-\Delta x_k/2, \Delta x_k/2]$ with centerpoint $x = 0$. By doing so, the math behind the reconstruction is dramatically simplified, and so we will hereafter assume that we are working over this domain. Further, we will assume that the grid is *uniform* so that $\Delta x_j = \Delta x$ for all j. Reconstructions based on non-uniform grids are generally a straightforward extension of the uniform case.

Perhaps the most intuitive method for determining the coefficients of (8.37) is to use a Taylor series expansion about the center of the cell ($x = 0$),

$$\psi_k(x) = \psi_k\big|_{x=0} + \left(\frac{\partial \psi_k}{\partial x}\right)\bigg|_{x=0} x + \frac{1}{2}\left(\frac{\partial^2 \psi_k}{\partial x^2}\right)\bigg|_{x=0} x^2 + \ldots + \frac{1}{p!}\left(\frac{\partial^p \psi_k}{\partial x^p}\right)\bigg|_{x=0} x^p + \mathscr{O}\left[(\Delta x)^{p+1}\right]. \quad (8.40)$$

By pairing terms of equal order, we obtain the association

$$c_k^{(0)} = \psi_k(0), \qquad c_k^{(i)} = \frac{1}{i!}\left(\frac{\partial^i \psi_k}{\partial x^i}\right)\bigg|_{x=0}. \quad (8.41)$$

Since we do not know the exact value of ψ_k or its derivatives, we must approximate these values using, for example, interpolated polynomials through known cell-averaged values.

Note that one must be careful in choosing the correct approximations to these derivatives to preserve high-order accuracy. Specifically, for (8.40) to be formally $\mathscr{O}[(\Delta x)^p]$ accurate, each of the derivatives $\partial^n \psi_k/\partial x^n$ must be approximated to order $\mathscr{O}[(\Delta x)^{p-n}]$, and $\psi_k(0)$ must be approximated to order $\mathscr{O}[(\Delta x)^p]$. The rationale behind this claim is as follows: When evaluating the reconstruction (8.40), each of the derivatives $\partial^n \psi_k/\partial x^n$ is multiplied by x^p, which must satisfy $|x|^p \leq (\Delta x)^p$. Hence, if $\partial^n \psi_k/\partial x^n$ is approximated to $\mathscr{O}[(\Delta x)^{n-p}]$ then each term in the series (8.40) is approximated to $\mathscr{O}[(\Delta x)^p]$. However, since $\psi_k(0)$ is not multiplied by any power of x, it must be approximated to full order-of-accuracy.

Finite-difference approximations

On averaging the Taylor series (8.40) over a cell A_k, we obtain

$$\frac{1}{\Delta x}\int_{-\Delta x/2}^{\Delta x/2} \psi_k(x)dx = \psi_k(0) + \frac{1}{12}\left(\frac{\partial^2 \psi_k}{\partial x^2}\right)\bigg|_{x=0} (\Delta x)^2 + \mathscr{O}\left[(\Delta x)^4\right]. \quad (8.42)$$

The left-hand-side of this expression is simply the cell average $\overline{\psi}_k$, which is known in a finite-volume context. The first term on the right-hand-side is the value of $\psi_k(x)$ evaluated at the cell-centerpoint and it is followed by higher-order terms. Hence, we can conclude that $\overline{\psi}_k$ is a $\mathscr{O}\left[(\Delta x)^2\right]$ approximation to the value of $\psi_k(x)$ evaluated at the centerpoint. This result implies that if we utilize finite-difference approximations to approximate derivatives of any order at $x = 0$, such approximations will only be valid up to $\mathscr{O}\left[(\Delta x)^2\right]$ in a finite-volume context.

The simplest finite-difference approximation is the piecewise-linear method (PLM), given by

$$\psi_k(x) = \overline{\psi}_k + \left(\frac{\partial \psi_k}{\partial x}\right)\bigg|_{x=0} x, \tag{8.43}$$

(van Leer, 1977) where $\partial \psi_k / \partial x$ is at least a first-order-accurate approximation to the derivative at $x = 0$. Some choices include an upwind discretization,

$$\left(\frac{\partial \psi_k}{\partial x}\right)\bigg|_{x=0} = \frac{\overline{\psi}_k - \overline{\psi}_{k-1}}{\Delta x} + \mathscr{O}(\Delta x), \tag{8.44}$$

or a centered discretization

$$\left(\frac{\partial \psi_k}{\partial x}\right)\bigg|_{x=0} = \frac{\overline{\psi}_{k+1} - \overline{\psi}_{k-1}}{2\Delta x} + \mathscr{O}\left[(\Delta x)^2\right]. \tag{8.45}$$

Either choice will lead to a scheme which is formally second-order accurate. Larger stencils can be chosen for the approximations to these derivatives, but they can only lead to reconstructions that are at most second-order-accurate. Nonetheless, with larger stencils total accuracy may improve significantly even though the formal order-of-accuracy will not.

The linear reconstruction drastically improves the error measures of finite-volume schemes, when compared to PCoM. This result is illustrated in Fig. 8.14 in terms of a von Neumann stability analysis of a finite-volume scheme based on PCoM and PLM (using the centered approximation (8.45)). In many large-scale atmospheric models PLM is still considered too diffusive and therefore even higher-order reconstructions are often considered.

Finite-difference schemes can also be utilized to obtain a third-order reconstruction, even in a finite-volume context. Rearranging (8.42), we can obtain an expression for the centerpoint value $\psi_k(0)$,

$$\psi_k(0) = \overline{\psi}_k - \frac{(\Delta x)^2}{24}\left(\frac{\partial^2 \psi_k}{\partial x^2}\right)\bigg|_{x=0} + \mathscr{O}\left[(\Delta x)^4\right], \tag{8.46}$$

which is a fourth-order-accurate approximation to the pointwise value of $\psi_k(0)$, as long as $\partial^2 \psi_k / \partial x^2$ is approximated to at least $\mathscr{O}\left[(\Delta x)^2\right]$. Combining this approximation with (8.40), we obtain a third-order (parabolic) reconstruction

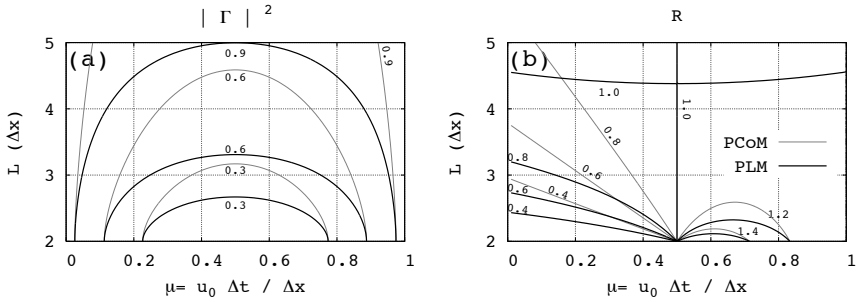

Fig. 8.14 The stability properties (see section 8.3.3 and/or Lauritzen 2007) of a one-dimensional finite-volume scheme based on PCoM (grey line) and PLM (black line), respectively. Note that in one dimension all finite-volume schemes discussed in this chapter are identical when using the same reconstruction method. (a) Squared modulus of the amplification factor ($|\Gamma|^2$) as a function of Courant number (x-axis) and wavelength L (y-axis). Hence (a) shows how much each wavelength is damped in one time-step as a function of Courant number. For a fixed Courant number μ the damping decreases monotonically as a function of wavelength L and $\lim_{L\to\infty}|\Gamma|^2 = 1$. For Courant number 0 or 1 the scheme is exact and hence $|\Gamma|^2 = 1$. (b) Same as (a) but for the relative phase speed (R), that is, how much each Fourier mode is accelerated or decelerated as a function of Courant number.

$$\psi_k(x) = \overline{\psi}_k + \left(\frac{\partial \psi_k}{\partial x}\right)\bigg|_{x=0} x + \frac{1}{2}\left(\frac{\partial^2 \psi_k}{\partial x^2}\right)\bigg|_{x=0}\left(x^2 - \frac{(\Delta x)^2}{12}\right) + \mathscr{O}\left[(\Delta x)^3\right], \tag{8.47}$$

when combined with simple finite-difference approximations of the form (8.45) and

$$\left(\frac{\partial^2 \psi_k}{\partial x^2}\right)\bigg|_{x=0} = \frac{\overline{\psi}_{k-1} - 2\overline{\psi}_k + \overline{\psi}_{k+1}}{(\Delta x)^2} + \mathscr{O}\left[(\Delta x)^2\right]. \tag{8.48}$$

In fact, it can be quickly verified that (8.47) also satisfies the cell-averaged property (8.38). This method has the highest formal order of accuracy that can be obtained by treating finite-volume methods in a finite-difference context. This choice of reconstruction was used by Laprise and Plante (1995).

Finite-volume approximations

To obtain approximations higher than third-order in accuracy, we must first take a step back and understand how finite-volume methods are formulated. First, recall that finite-volume methods use cell-averaged values, which implies that the underlying scalar field is not known point-by-point. Instead, it is cell-averaged values that are known exactly

$$\overline{\psi}_k = \frac{1}{\Delta x}\int_{-\Delta x/2}^{\Delta x/2} \psi_k(x)dx. \tag{8.49}$$

Hence, in the context of finite-volume methods, high-order sub-grid-scale reconstructions cannot be interpolated through specific points (as with finite-difference methods), but must instead satisfy certain cell-averaged properties.

To build a reconstruction that utilizes cell-averages, one generally defines a *cumulative mass function* $W(x)$ via

$$W(x) = \int_{x_{k-j-1/2}}^{x} \psi_k(\tilde{x}) d\tilde{x}, \tag{8.50}$$

where $x_{k-j-1/2}$ denotes the left-side edge of cell A_{k-j}. Now, observe

$$\begin{aligned} W(x_{k-j-1/2}) &= 0, \\ W(x_{k-j+1/2}) &= \Delta x \left(\overline{\psi}_{k-j} \right), \\ W(x_{k-j+3/2}) &= \Delta x \left(\overline{\psi}_{k-j} + \overline{\psi}_{k-j+1} \right), \\ &\vdots \end{aligned}$$

Over such a set of consecutive cells one can then define an interpolating polynomial of degree m that approximates the exact cumulative mass function $W(x)$. We denote this approximation by $\tilde{W}(x)$. Finally, we observe that in accordance with the fundamental theorem of Calculus, differentiating (8.50) gives

$$\frac{dW}{dx}(x) = \psi_k(x). \tag{8.51}$$

By evaluating the first derivative of $\tilde{W}(x)$ at a given point, we actually obtain a $\mathcal{O}\left[(\Delta x)^{m-1}\right]$ approximation to the underlying field $\psi_k(x)$ from its cell-averages. This method can then be used to reconstruct $\psi_k(x)$ at any point and, by taking additional derivatives of $\tilde{W}(x)$, its corresponding derivatives.

Alternatively, one can obtain an identical reconstruction by enforcing the cell-averaged constraint on an interpolating polynomial in neighboring cells (Zerroukat et al, 2002). That is, a polynomial $\widehat{\psi}_k(x)$ of degree p that exactly satisfies the mass-conservation constraint not only in cell k but also in p adjacent cells:

$$\int_{x_{j-1/2}}^{x_{j+1/2}} \widehat{\psi}_k(x)\, dx = \overline{\psi}_j \Delta x, \quad j = \left(k - \frac{p}{2}\right) .. \left(k + \frac{p}{2}\right), \tag{8.52}$$

for p even and

$$\int_{x_{j-1/2}}^{x_{j+1/2}} \widehat{\psi}_k(x)\, dx = \overline{\psi}_j \Delta x, \quad j = \left(k - \frac{p+1}{2}\right) .. \left(k + \frac{p-1}{2}\right), \tag{8.53}$$

for p odd.

Either method will yield an identical reconstruction ($\tilde{W}(x) = \widehat{\psi}_k(x)$), although the latter is more adaptable to two dimensions and beyond.

If we utilize the aforementioned procedure over a 3-cell stencil (consisting of cells $k-1$, k and $k+1$), we will exactly obtain (8.45), (8.46) and (8.48). However, beyond 3 cells, the finite-difference and finite-volume reconstructions will differ substantially. For instance, over a centered 5-cell stencil, we obtain approximations

$$\psi_k(0) = \frac{9\overline{\psi}_{k-2} - 116\overline{\psi}_{k-1} + 2134\overline{\psi}_k - 116\overline{\psi}_{k+1} + 9\overline{\psi}_{k+2}}{1920} + \mathscr{O}\left[(\Delta x)^6\right],$$
$$\left(\frac{\partial \psi_k}{\partial x}\right)\Bigg|_{x=0} = \frac{5\overline{\psi}_{k-2} - 34\overline{\psi}_{k-1} + 34\overline{\psi}_{k+1} - 5\overline{\psi}_{k+2}}{48\,\Delta x} + \mathscr{O}\left[(\Delta x)^5\right],$$
etc.

High-order reconstructions of this type were adopted for a shallow-water model by Ullrich et al (2010).

Symmetric finite-volume schemes

In all the methods so far discussed, we have not touched on the issue of continuity between cells. In fact, all of the methods we have described so far do not enforce any sort of continuity between reconstructions in neighboring cells.

As we have seen so far, as the order of the reconstruction polynomial is increased, more options for how to approximate the coefficients $c_k^{(i)}$ are available. Continuity at edges can be enforced (over an arbitrary scalar field) if we adopt a reconstruction that is at least parabolic, *i.e.*

$$\psi_k(x) = c_k^{(0)} + c_k^{(1)} x + c_k^{(2)} x^2. \tag{8.54}$$

Since we have three degrees of freedom in this polynomial, we can choose to enforce $\psi_k(-\Delta x/2) = \psi_k^L$ and $\psi_k(\Delta x/2) = \psi_k^R$, where ψ_k^L and ψ_k^R are reconstructed values at the left- and right- edges, respectively. These are purposely chosen to be consistent between neighboring cells, which gives us the desired continuity restriction. With our remaining degree of freedom we enforce the cell-averaged condition (8.38).

This scheme is the well-known piecewise-parabolic method (PPM) of Colella and Woodward (1984). To obtain edgepoint values ψ_k^L and ψ_k^R, PPM makes use of the finite-volume formulation discussed earlier, taken over four cells and evaluated at the cell edgepoint, which gives

$$\psi_k^R = \frac{7}{12}(\overline{\psi}_k + \overline{\psi}_{k+1}) - \frac{1}{12}(\overline{\psi}_{k+2} + \overline{\psi}_{k-1}) + \mathscr{O}\left[(\Delta x)^4\right], \tag{8.55}$$

(also see Zerroukat et al (2002)) and $\psi_{k+1}^L = \psi_k^R$. In terms of the coefficients $c_k^{(i)}$, this reconstruction can be written as

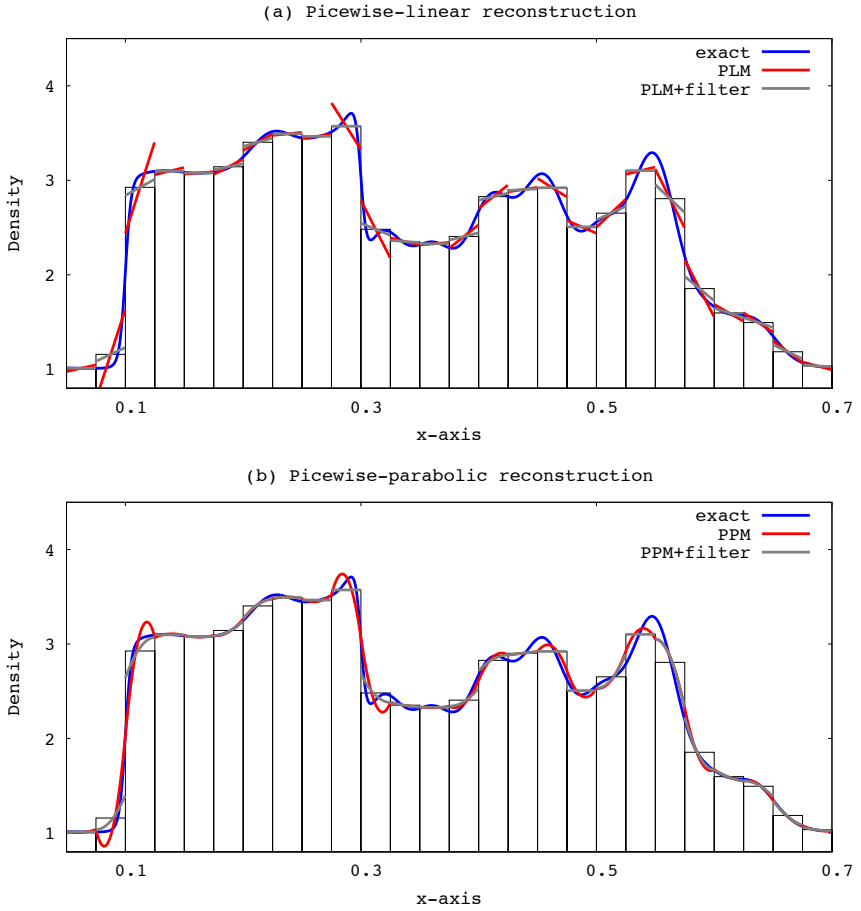

Fig. 8.15 Reconstructions for the irregular signal of Smolarkiewicz and Grabowski (1990, blue line) using the (a) piecewise-linear method (PLM) and (b) the piecewise parabolic method (PPM) with reconstruction function filter (grey) and without (red). The filter for PLM is the MINMOD limiter (see text) with theta=1 and the PPM limiter is the original filter presented in Colella and Woodward (1984).

$$
\begin{aligned}
c_k^{(0)} &= \overline{\psi}_k - (\Delta x)^2 \frac{c_k^{(2)}}{12}, \\
c_k^{(1)} &= \frac{1}{\Delta x}\left[\frac{2}{3}\left(\overline{\psi}_{k+1} - \overline{\psi}_{k-1}\right) - \frac{1}{12}\left(\overline{\psi}_{k+2} - \overline{\psi}_{k-2}\right)\right], \\
c_k^{(2)} &= \frac{1}{2(\Delta x)^2}\left[-5\overline{\psi}_k + 3\left(\overline{\psi}_{k+1} + \overline{\psi}_{k-1}\right) - \frac{1}{2}\left(\overline{\psi}_{k+2} + \overline{\psi}_{k-2}\right)\right].
\end{aligned}
$$

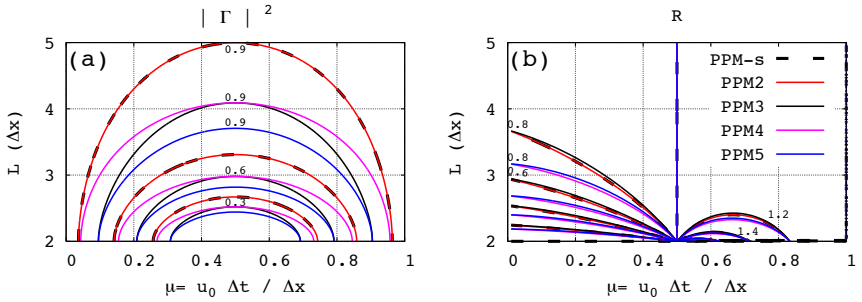

Fig. 8.16 Same as Fig. 8.14 but for PPM using different estimates for the edge values (solid lines) as well as PPM-s (dashed line). PPM-s is the sub-grid-cell reconstruction method based on the method of Laprise and Plante (1995), that is, using (8.52) with $p = 2$ to determine the sub-grid-cell reconstruction function.

All of the coefficients $c_k^{(i)}$ in this case approximate $\psi_k(x)$ and its derivatives to $\mathcal{O}\left[(\Delta x)^4\right]$.

The approximation to ψ_k^L in (8.55) and ψ_k^R are fourth-order accurate for uniform grids. Obviously, one could also derive second, third, fourth, fifth or sixth-order accurate estimations by fitting a linear, parabolic, cubic, quartic and quintic polynomial so that (8.50) or (8.52-8.53) is satisfied in 2, 3, 4, 5 and 6 adjacent cells, respectively. We will refer to PPM based on second, third, fourth, fifth-order edge value estimates as PPM2, PPM3, PPM4, PPM5, respectively. In this context PPM and PPM4 refer to the same reconstruction.

In terms of p-exactness the edge estimates must be at least third-order for the PPM to exactly reconstruct a global parabola. Hence PPM2 is not p-exact (p=2) whereas PPM3, PPM4, and PPM5 are. It is noted that PPM4 is significantly more accurate than PPM3 in terms of a Von Neuman stability analysis (Fig. 8.16) whereas PPM5 only gives modest increases in accuracy. Obviously PPM5 needs a larger halo than PPM4. As a consequence, the potential increase in cost associated with the use of larger stencils has likely been a significant factor in determining the widespread adoption of PPM4 over these other schemes. More discussion on edge-value estimates is given in White and Adcroft (2008).

One could naturally ask the question why should one not use the highest-order polynomial that can be approximated with a given halo (stensil)? For example, the cubic polynomial used to estimate the edge value in PPM4 could be used as the reconstruction function, $\psi_k(x) = \widehat{\psi}_k(x)$. While this might improve the accuracy of the scheme, it will make filtering and integration over overlap-areas more cumbersome and computationally expensive, as compared to sticking to a parabola with high-order edge-value estimates (PPM4).

Reconstructions based on polynomials of degree higher than 2 have been proposed in the literature but have not been widely adopted in transport schemes as of the time of writing. Zerroukat et al (2002) introduced a symmetric piecewise-cubic method (PCM), along with advanced filtering techniques (Zerroukat et al, 2005),

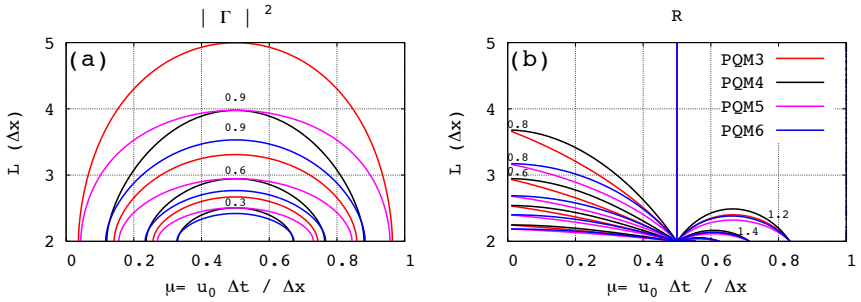

Fig. 8.17 Same as Fig. 8.16 but for PQM.

and White and Adcroft (2008) proposed a symmetric piecewise-quartic method (PQM) based on polynomials of degree 4. As for the PPM the edge-value estimate is paramount for the accuracy of the scheme (see, e.g., Fig. 8.17). However, even for the most accurate PQM6 the increase in accuracy (in terms of a Von Neumann analysis) is modest compared to PPM4 given the increase in the halo size. Also to consider is that polynomials of degree 3 (PCM) and 4 (PQM) can have 2 and 3 extrema within a grid cell making it harder to filter such polynomials compared to a (relatively low-order) parabola.

Piecewise quadratic splines.

An interesting variant on the reconstruction methods discussed so far, and also based on parabolas, is the piecewise quadratic spline method (Zerroukat et al 2006) and higher-order extensions such as those presented in Zerroukat et al (2010). Instead of only enforcing C^0 continuity across cell edges also the first derivative of the reconstruction is constrained to be continuous, i.e. the reconstruction is C^1 across cell edges. Enforcing continuity in the derivatives of the reconstruction functions at cell boundaries results in an implicit system of equations for the polynomial coefficients. When written in matrix form, however, the matrix that needs to be inverted has a tri-diagonal form.

In idealized test cases using the scheme of Zerroukat et al (2002) the piecewise spline reconstruction method is superior to PPM while being 40% more efficient in terms of number of operations (Zerroukat et al, 2007). The price to pay, in terms of a parallel computational environment, is that splines are inherently global since the inversion of a global tri-diagonal matrix is necessary.

Essentially non-oscillatory (ENO) reconstructions.

Essentially non-oscillatory reconstructions were originally developed by Harten et al (1987) for shock hydrodynamics problems. This approach is particularly in-

teresting since it leads to a reconstruction that is (under most circumstances) monotonic and positive. The ENO scheme works by applying either a finite-difference or finite-volume approach (as discussed earlier) on a variety of stencils. The reconstruction that satisfies some least-oscillatory property, among all possible stencils, is then chosen to give the 'true' reconstruction. The main drawback of this approach is that it requires a large stencil in order to obtain the same order of accuracy as 'vanilla' finite-difference or finite-volume methods.

Least-squares

The least-squares technique is one of the few approaches available for obtaining approximate reconstructions on unstructured grids. Under this method, we introduce some quantification of the misfit between the reconstruction (8.37) and the known cell-averages, usually given by the square of the difference between the cell-averages of the reconstruction and the known cell-averages. The misfit is then minimized over all possible reconstructions in order to give the "best possible" reconstruction. An example of a Cartesian finite-volume scheme on an unstructured grid based on the least-squares technique can be found in Barth and Frederickson (1990).

One-dimensional reconstruction limiters/filters

As discussed in section 8.3.6, it is desirable that a transport scheme utilizes physically realizable reconstructions. There are two ways to achieve this goal, either *a priori* by filtering the sub-grid-cell reconstruction function so that it only takes physically realizable values, or *a posteriori* by limiting prognosed cell averages or by altering the fluxes individually. In the context of an upstream semi-Lagrangian scheme flux-limiting is obviously not an option. For Eulerian schemes one may apply *a priori* filters or flux-limiters to provide physically realizable solutions. *A priori* filters are also referred to as slope-limiters as they act directly on the sub-grid-scale reconstruction function.

The PLM, usually based on (8.44) or (8.45), may violate monotonicity as illustrated in Fig. 8.15(a). Monotonicity can be enforced by replacing the reconstructed derivative with some weighted average of the upwind and downwind approximations. Many such combinations exist, including MINMOD, Superbee (Roe, 1985), and monotone central (van Leer, 1977), to name a few (see, for example, Toro 1999). It is beyond the scope of this chapter to provide a comprehensive review of these filters but they all seek to blend the derivative estimates, as hinted above, to obtain the least diffusive monotone solution.

As illustrated on Fig. 8.15(b) PPM4 is also non-monotone without the application of filters. The seminal paper of Colella and Woodward (1984) constrains the reconstruction so that the entire sub-grid-scale reconstruction is bounded by the cell-averages of the neighboring cells (or is reduced to a constant when the reconstruction is a local extrema). See Figure 8.15(b) for an example. This technique for

filtering the reconstruction has the tendency to "cut off" or flatten smooth, physical maxima and minima. Several approaches have been proposed to retain physical extrema while filtering out spurious grid-scale noise (see, for example, van Albada et al (1982), Zerroukat et al (2005), Liu et al (2007) and Colella and Sekora (2008)). If miniscule over- and undershoots can be tolerated, less invasive filters can be designed using (W)ENO-type methods where the user-specified filter is applied only when a smoothness metric exceeds a certain threshold (Blossey and Durran, 2008). Achieving high-order accuracy and physical realizable prognosed values (monotonicity) is very challenging and deserves a chapter on its own for a comprehensive discussion. We will not discuss reconstruction filtering further, although it has profound impact on the diffusion and dispersion properties of a scheme at small scales.

8.5.2.2 Two-dimensional reconstruction functions

Two-dimensional reconstructions can be obtained using nearly direct generalizations of the methods presented in section 8.5.2.1. In fact, for second-order accurate schemes that use a linear reconstruction the linear derivatives can be calculated in each direction independently (dimension-splitting).

Reconstruction problem formulation

The two-dimensional reconstruction problem for a finite-volume scheme utilizing a polynomial basis is analogous to the one-dimensional case: Given discrete cell-averaged values $\overline{\psi}_k$ over cells A_k, determine coefficients $c^{(i,j)}$, $i+j \leq p$ (i and j are 0 or positive integers), so that

$$\psi_k(x,y) = \sum_{i+j\leq p} c_k^{(i,j)} x^i y^j, \tag{8.56}$$

is an approximation to the underlying field ψ in cell A_k. The cell-averaged property in two dimensions then reads,

$$\int_{A_k} \psi_k(x,y)\, dA = \overline{\psi}_k \Delta A_k. \tag{8.57}$$

Again we can choose to shift the reconstruction so that, for simplicity, A_k has a centroid located at $(x,y) = (0,0)$.

Piecewise Constant Method (two dimensions)

The extension of the PCoM to two dimensions is trivial, given by

$$\psi_k(x,y) = \overline{\psi}_k. \tag{8.58}$$

This scheme suffers from the same deficiencies as discussed in the one-dimensional case, and so is not discussed further here.

Piecewise Linear Method (two dimensions)

The two-dimensional piecewise linear reconstruction can be written as

$$\psi_k(x,y) = \overline{\psi}_k + c_k^{(1,0)}x + c_k^{(0,1)}y. \tag{8.59}$$

Any choice of $c_k^{(1,0)}$ and $c_k^{(0,1)}$ will yield a mass-conservative reconstruction and, as with the one-dimensional PLM, $c_k^{(1,0)}$ and $c_k^{(0,1)}$ correspond to the components of the gradient along each coordinate direction at the cell centroid,

$$c_k^{(1,0)} = \left(\frac{\partial \psi_k}{\partial x}\right)\Bigg|_{(x,y)=(0,0)},$$
$$c_k^{(0,1)} = \left(\frac{\partial \psi_k}{\partial y}\right)\Bigg|_{(x,y)=(0,0)}.$$

For this method, the gradient can be limited as in the one-dimensional case (see, e.g., Dukowicz and Baumgardner, 2000).

High-order reconstructions (two dimensions)

True third-order and higher schemes require some method of incorporating cross-derivatives in order to be formally third-order accurate. For example, a true third-order parabolic reconstruction could make use of a reconstruction of the form

$$\begin{aligned}\psi_k(x,y) = \overline{\psi}_k + c_k^{(1,0)}x + c_k^{(0,1)}y \\ + c_k^{(2,0)}\left(x^2 - \frac{(\Delta x)^2}{12}\right) + c_k^{(1,1)}xy + c_k^{(0,2)}\left(y^2 - \frac{(\Delta y)^2}{12}\right),\end{aligned} \tag{8.60}$$

where $c_k^{(1,0)}$, $c_k^{(0,1)}$, $c_k^{(2,0)}$, $c_k^{(0,2)}$, and $c_k^{(1,1)}$ are obtained by again approximating the derivatives of ψ. Note that $c^{(0.0)}$ does not equal the cell average $\overline{\psi}$ but includes more terms to ensure the mass-conservation property. Extensions of this form are described in Nair and Machenhauer (2002) and Ullrich et al (2010). It has been shown that the loss of accuracy attributed to neglecting the cross-derivative term $c_k^{(1,1)}$ can be large, but is less significant on grids of low resolution (Lauritzen et al, 2010).

Piecewise Parabolic Method (two dimensions)

A rigorous extension of the PPM method introduced by Colella and Woodward (1984) would require the fully two dimensional biparabolic polynomials to be continuous across cell-borders at selected points and/or in some average sense.

One such extension was developed by Rančić (1992), who chose

$$\psi(x,y) = \phi_2(y)x^2 + \phi_1(y)x + \phi_0(y), \tag{8.61}$$

where

$$\phi_0(y) = \phi_{02}y^2 + \phi_{01}y + \phi_{00}, \tag{8.62}$$
$$\phi_1(y) = \phi_{12}y^2 + \phi_{11}y + \phi_{10}, \tag{8.63}$$
$$\phi_2(y) = \phi_{22}y^2 + \phi_{21}y + \phi_{20}. \tag{8.64}$$

This reconstruction has nine degrees of freedom, which are restricted by satisfying (i) the cell-averaged constraint (8.57) in cell k, (ii) equal average values along each of the four edges of the quadrilateral cells, and (iii) continuity at the corner points of each cell. These restrictions lead to 9 constraints, and hence define a unique reconstruction. Note that the reconstruction is not globally continuous. We refer to Rančić (1992) for further details on this algorithm.

Extensions to irregular grids

All of the methods described above are tied to quadrilateral (orthogonal) meshes and the extension to triangular, hexagonal and other grids where the cells do not have exactly four vertices, is not obvious. The authors are not aware of any rigorous extensions of PPM to such grids where continuity across cell borders is enforced. In this case enforcement of the cell-average property is more difficult, and requires special treatment of the parabolic terms. For instance, we must have

$$c_k^{(0,0)} = \overline{\psi}_k + c_k^{(2,0)}\left[x^2 - m_k^{(2,0)}\right] + c_k^{(0,2)}\left[y^2 - m_k^{(0,2)}\right] + c^{(1,1)}\left[xy - m_k^{(1,1)}\right], \tag{8.65}$$

(Ullrich et al, 2009) where $m_k^{(i,j)}$ are the area-averaged higher-order moments

$$m_k^{(i,j)} = \frac{1}{\Delta A_k}\int_{A_k} x^i y^j \, dA.$$

Approximation of the derivative terms may be difficult on irregular grids. For grids where finite-difference approximations to the derivatives are not obvious to compute, as is the case for completely unstructured grids, one might use a two-dimensional extension of the Laprise and Plante (1995) method. That is, enforce the mass-conservation constraint not only in cell k but in a set of adjacent cells. For grids in which cell k has a variable number of adjacent neighbors this approach may not

be optimal. In such cases a least-squares approach might be a more natural choice to avoid biases introduced by excluding some adjacent cells and not others. When using a least squares method one may chose to optimize the approximation to the coefficients not just to mass-conservation in adjacent cells but also to p-exactness for example (see, e.g., Barth and Frederickson, 1990).

Two-dimensional limiters / filters

Reconstruction function filtering in two-dimensions is significantly more complicated than in one dimension, simply because a two-dimensional polynomial of degree 2 (a parabolic reconstruction) can possess an extrema within a cell, along a cell boundary, or at a corner-point (all of which must be checked). Hence, filtering comes in two flavors: Dimensionally split filtering and fully two-dimensional approaches.

The dimensional split approach simply applies the one-dimensional filters presented in section 8.5.2.1 in each coordinate direction. However, by doing so the entire reconstruction ψ_k is not guaranteed to be monotonic within A_k. Specifically, there are no guarantees of monotonicity at cell corner-points where the reconstruction in each coordinate direction is additive (Lauritzen et al, 2006).

Strict monotonicity at all points within a cell can be guaranteed using the fully two-dimensional approach of Barth and Jespersen (1989), which can also be applied to unstructured grids. This filter guarantees strict monotonicity of linear reconstructions by first determining where a given linear reconstruction has extrema (this is typically the cell corner-points), and then rescaling the linear derivatives so that the linear reconstruction is monotonic with respect to its neighbors. This approach was also extended to parabolic (third-order) reconstructions by Ullrich et al (2009), which applies rescaling to both linear and high-order derivatives. If strict monotonicity is not necessary, a WENO-type criterion can be used to identify places in which a filter should be applied. An extension of the one-dimensional WENO-filtering in Blossey and Durran (2008) can be found in Harris et al (2010).

For flux-limiting the most widely used method is flux-corrected transport (FCT) introduced by Zalesak (1979). As in one dimension it seeks to find the optimal "blending" of a monotone flux and a high-order non-monotone flux. FCT is described in detail in Durran (1999) and hence not repeated here.

8.5.3 Practical integration over areas

For the approximation of the overlap integrals in (8.26) and (8.33) we have only discussed how to approximate the overlap areas and how to do reconstructions so far. It remains to be shown how to go about integrating the sub-grid-scale reconstruction function over that area. If the sides of the overlap areas are aligned with the coordinate lines, direct integration is usually straightforward since the integrals ef-

fectively reduce to one dimension (see, for example, Nair and Machenhauer (2002)). However, if the overlap area is allowed to be an arbitrary polygon the integration is more involved. There are basically two approaches that exactly integrate polynomial functions over polygons. Firstly, direct integration over overlap areas using Gaussian quadrature. Secondly, the area-integrals can be converted into line-integrals via Gauss-Green's theorem.

Both of these approaches are discussed below. We assume that the overlap cell sides are straight lines with arbitrary orientation and that the overlap area $a_{k\ell}$ is simply connected. This is the most general case. Mathematically the problem is stated as follows: Given a reconstruction function in cell A_ℓ which is a polynomial, say of order 3,

$$\psi_\ell(x,y) = \sum_{i+j\leq 2} c_\ell^{(i,j)} x^i y^j, \tag{8.66}$$

where $c_\ell^{(i,j)}$ are reconstruction coefficients, compute the integral

$$\int_{a_{k\ell}} \psi_\ell(x,y) dA. \tag{8.67}$$

8.5.3.1 Direct integration using Gaussian quadrature

For the direct integration using Gaussian quadrature it is often convenient to break up $a_{k\ell}$ into triangles which is the case we will discuss here. So, for simplicity, suppose the overlap area is already an arbitrary triangle[18] with vertices located at $x_{k\ell,h}$, $y_{k\ell,h}$, $h = 1,2,3$, and numbered counter-clockwise. Exact integration of the polynomial (8.66) can be achieved using Gaussian quadrature which approximates the integral in terms of a weighted sum of functional evaluations at quadrature points. The quadrature points are

$$(x_{k\ell}^{(a)}, y_{k\ell}^{(a)}) = \tfrac{1}{6}\left(4x_{k\ell,1} + x_{k\ell,2} + x_{k\ell,3}, 4y_{k\ell,1} + y_{k\ell,2} + y_{k\ell,3}\right), \tag{8.68}$$

$$(x_{k\ell}^{(b)}, y_{k\ell}^{(b)}) = \tfrac{1}{6}\left(x_{k\ell,1} + 4x_{k\ell,2} + x_{k\ell,3}, y_{k\ell,1} + 4y_{k\ell,2} + y_{k\ell,3}\right), \tag{8.69}$$

$$(x_{k\ell}^{(c)}, y_{k\ell}^{(c)}) = \tfrac{1}{6}\left(x_{k\ell,1} + x_{k\ell,2} + 4x_{k\ell,3}, y_{k\ell,1} + y_{k\ell,2} + 4y_{k\ell,3}\right). \tag{8.70}$$

(Dukowicz and Baumgardner, 2000) and the integral of $\psi_\ell(x,y)$ over the overlap triangle $a_{k\ell}$ is given by

$$\int_{a_{k\ell}} \psi_\ell(x,y)\, dA = \frac{\Delta a_{k\ell}}{3}\left[\psi_\ell(x_{k\ell}^{(a)}, y_{k\ell}^{(a)}) + \psi_\ell(x_{k\ell}^{(b)}, y_{k\ell}^{(b)}) + \psi_\ell(x_{k\ell}^{(c)}, y_{k\ell}^{(c)})\right], \tag{8.71}$$

where $\Delta a_{k\ell}$ is the area of $a_{k\ell}$

$$\Delta a_{k\ell} = \frac{1}{2}\left[(x_{k\ell,2} - x_{k\ell,1})(y_{k\ell,3} - y_{k\ell,1}) - (y_{k\ell,2} - y_{k\ell,1})(x_{k\ell,3} - x_{k\ell,1})\right]. \tag{8.72}$$

[18] note that any area with straight line sides can be broken up into triangles

Note that the quadrature points only have to be computed once for each overlap area and can then be re-used for each additional tracer (since all tracers follow the same trajectories/areas). For flux-form transport schemes efficient algorithms can be designed that decompose the overlap areas into triangles if the flux-areas are confined to nearest neighbors (Dukowicz and Baumgardner, 2000). For longer time-steps where the flux-areas may span several Eulerian cells not sharing a face with the flux-face, the decomposition into triangles is more complicated. In such situations it may be more convenient to use the line-integral approach described next.

8.5.3.2 Converting area-integrals into line-integrals

This approach was originally introduced by Dukowicz (1984) and Dukowicz and Kodis (1987) in numerical schemes: For the simply connected overlap area $a_{k\ell}$ (not necessarily a triangle but any polygon) the following integral equation holds,

$$\iint_{a_{k\ell}} \psi_\ell(x,y)\,dA = \oint_{\partial a_{k\ell}} [P\,dx + Q\,dy]\,, \tag{8.73}$$

where $\partial a_{k\ell}$ is the boundary of $a_{k\ell}$. The potentials $P = P(x,y)$ and $Q = Q(x,y)$ are chosen such that they satisfy

$$-\frac{\partial P}{\partial y} + \frac{\partial Q}{\partial x} = \psi_\ell(x,y).$$

The integral of the polynomial reconstruction function $\psi_\ell(x,y)$ in (8.66) can be written as

$$\int_{a_{k\ell}} \psi_\ell(x,y)\,dA = \sum_{i+j\le 2} c_\ell^{(i,j)} w_{k\ell}^{(i,j)}, \tag{8.74}$$

where $c_\ell^{(i,j)}$ are the reconstruction function coefficients and $w_{k\ell}^{(i,j)}$ are weights given by

$$w_{k\ell}^{(0,0)} = \frac{1}{2}\sum_{h=1}^{N_h}\left(x_{k\ell,h}+x_{k\ell,h-1}\right)\left(y_{k\ell,h}-y_{k\ell,h-1}\right), \tag{8.75}$$

$$w_{k\ell}^{(1,0)} = \frac{1}{6}\sum_{h=1}^{N_h}\left(x_{k\ell,h}^2+x_{k\ell,h}x_{k\ell,h-1}+x_{k\ell,h-1}^2\right)\left(y_{k\ell,h}-y_{k\ell,h-1}\right), \tag{8.76}$$

$$w_{k\ell}^{(0,1)} = -\frac{1}{6}\sum_{h=1}^{N_h}\left(y_{k\ell,h}^2+y_{k\ell,h}y_{k\ell,h-1}+y_{k\ell,h-1}^2\right)\left(x_{k\ell,h}-x_{k\ell,h-1}\right), \tag{8.77}$$

$$w_{k\ell}^{(2,0)} = \frac{1}{12}\sum_{h=1}^{N_h}\left(x_{k\ell,h}+x_{k\ell,h-1}\right)\left(x_{k\ell,h}^2+x_{k\ell,h-1}^2\right)\left(y_{k\ell,h}-y_{k\ell,h-1}\right), \tag{8.78}$$

$$w_{k\ell}^{(0,2)} = -\frac{1}{12}\sum_{h=1}^{N_h}\left(y_{k\ell,h}+y_{k\ell,h-1}\right)\left(y_{k\ell,h}^2+y_{k\ell,h-1}^2\right)\left(x_{k\ell,h}-x_{k\ell,h-1}\right), \tag{8.79}$$

$$w_{k\ell}^{(1,1)} = \frac{1}{24}\sum_{h=1}^{N_h}\Bigg\{\Big[y_{k\ell,h}\left(3x_{k\ell,h}^2+2x_{k\ell,h}x_{k\ell,h-1}+x_{k\ell,h-1}^2\right)+ y_{k\ell,h-1}\left(x_{k\ell,h}^2+2x_{k\ell,h}x_{k\ell,h-1}+3x_{k\ell,h-1}^2\right)\Big] \left(y_{k\ell,h}-y_{k\ell,h-1}\right)\Bigg\}, \tag{8.80}$$

and

$$(x_{k\ell,h}, y_{k\ell,h}), \quad h = 1,\ldots,N_h \tag{8.81}$$

are the coordinates for the sides of the overlap area $a_{k\ell}$ numbered counter-clockwise. So $N_h = 3$ for triangular overlap areas, $N_h = 4$ for quadrilateral $a_{k\ell}$'s etc. Note that $(x_{k\ell,h-1}, y_{k\ell,h-1})$ and $(x_{k\ell,h}, y_{k\ell,h})$ are contiguous points (defining a line segment) and the index h is cyclic so that $h = 0$ equals $h = N_h$.

The weights $w_{k\ell}^{(i,j)}$ given in equations (8.75-8.80) have been derived by using (8.73) with the following pairs $(P^{(i,j)}, Q^{(i,j)})$

$$\left(P^{(0,0)} = 0,\ Q^{(0,0)} = x\right),$$
$$\left(P^{(1,0)} = 0,\ Q^{(1,0)} = \tfrac{x^2}{2}\right),$$
$$\left(P^{(0,1)} = -\frac{y^2}{2},\ Q^{(0,1)} = 0\right),$$
$$\left(P^{(2,0)} = 0,\ Q^{(2,0)} = \tfrac{x^3}{3}\right),$$
$$\left(P^{(0,2)} = -\frac{y^3}{3},\ Q^{(0,2)} = 0\right),$$
$$\left(P^{(1,1)} = 0,\ Q^{(1,1)} = \tfrac{x^2 y}{2}\right).$$

The choice of P and Q is not unique and can often be chosen for convenience. Here we haven chosen P and Q as in Bockman (1989). Note that the integration of the polynomials is exact.

Using the line-integral approach the final discretized transport scheme in Lagrangian and Eulerian form can be written as

$$\overline{\psi}_k^{n+1}\,\Delta A_k = \sum_{\ell=1}^{L_k} \int_{a_{k\ell}} \psi_\ell(x,y)\,dA = \sum_{\ell=1}^{L_k} \left[\sum_{i+j<2} c_\ell^{(i,j)} w_{k\ell}^{(i,j)} \right], \tag{8.82}$$

and

$$\overline{\psi}_k^{n+1}\,\Delta A_k = \overline{\psi}_k^{n}\,\Delta A_k + \sum_{\tau=1}^{4} \left[\sum_{\ell=1}^{L_k^\tau} F_{k\ell}^\tau \right] = \overline{\psi}_k^{n}\,\Delta A_k + \sum_{\tau=1}^{4} \left\{ \sum_{\ell=1}^{L_k^\tau} \left[\sum_{i+j<2} c_\ell^{(i,j)} w_{k\ell}^{(i,j)}(\tau) \right] \right\}, \tag{8.83}$$

respectively, where the individual overlap fluxes are written as

$$F_{k\ell}^\tau = s_{k\ell}^\tau \int_{a_{k\ell}^\tau} \psi_\ell(x,y)\,dA. \tag{8.84}$$

For each overlap area the sign-function $s_{k\ell}^\tau$ is $+1$ for inflow and -1 for outflow. The subscript ℓ in s_ℓ^τ is added to handle situations where there is both inflow and outflow for a face (see Harris et al, 2010, for details).

It is worth noting the separation of the weights $w_{k\ell}^{(i,j)}$ from the reconstruction coefficients $c_\ell^{(i,j)}$ in (8.82) and (8.83). In practice this separation implies that once the weights have been computed they can be reused for the integral of each additional tracer distribution. Hence the transport of additional tracers reduces to the multiplication of precomputed weights and reconstruction coefficients.

8.5.3.3 Extension to spherical geometry

Extending the aforementioned approaches to spherical geometry generally compounds the complexity of the problem, since extra care must be taken when metric terms are present. So instead of having interpolate a polynomial a more complicated function must be integrated

$$\int\int_{a_{k\ell}} g(\alpha,\beta)\,\psi_\ell(\alpha,\beta)\,d\alpha\,d\beta, \tag{8.85}$$

where (α,β) is the coordinate for the computational space chosen for the integration[19] and $g(\alpha,\beta)$ is the metric term. For example, if one chooses geographic coordinates $(\alpha,\beta) = (\lambda,\theta)$, where λ is the longitude and θ is latitude, and then the

[19] for simplicity we only consider two-dimensional computational spaces although one may also use three-dimensional Cartesian coordinates for horizontal problems on the sphere

metric term is $g = R^2 \cos(\theta)$ where R is the radius of the Earth. So instead of having to integrate a polynomial a much more complicated function must integrated. In general, exact integration is no longer possible as was the case in Cartesian geometry. There are, however, some special cases where direct integration is possible (discussed below).

The choice of coordinate system in which the integration is performed has implications on how the sides of $a_{k\ell}$ are approximated on the sphere and how accurate the reconstruction is. Here we will focus on the former. In Cartesian geometry the most general approximation to cell sides seems to be straight lines. The spherical extension of that is to approximate cell sides with great-circle arcs which seems the most general and accurate approach (at least in the case where the Eulerian cells are constructed from great-circle arcs). Hence, in the following we assume that great-circle arcs are the most accurate approximations to $a_{k\ell}$.

In the widely used Spherical Coordinate Remapping and Interpolation Package (SCRIP) proposed by Jones (1999) the sides of $a_{k\ell}$ are approximated with straight line segments in latitude-longitude coordinates (*i.e.* line segments of the form $\theta = a\lambda + b$). So for sides that are parallel to longitudes (which are great-circle arcs) and latitudes (which are small circle arcs) the representation of the cell sides is exact. However, for any other orientation it is not. While the error in cell side approximation is small near the Equator the errors may become significant in the polar regions (see Fig. 9 in Lauritzen and Nair (2008)). A way to alleviate this problem is to rotate the overlap area to the Equator. Using Gauss-Green's theorem the integration here can be performed exactly whereas direct integration using Gaussian quadrature will not be exact due to the metric term.

An alternative approach is to use the gnomonic coordinate as the computational space. The gnomonic projection was designed so that connecting any two points with a straight line in that computational space will mirror a great-circle arc on the sphere. Another beneficial property of this computational space is that exact integration of (8.85) is possible along coordinate lines in the gnomonic coordinate system when applying the Gauss-Green's theorem (Ullrich et al, 2009). For lines not parallel to the coordinate lines the potentials that need to be integrated in the line-integrals can be evaluated/approximated using one-dimensional Gaussian quadrature (Lauritzen et al, 2010). Again, direct integration will always be inexact due to the gnomonic metric terms.

8.6 Extension to three dimensions

The discussion so far has been limited to two spatial dimensions and we will only briefly discuss three-dimensional schemes, as a more thorough discussion would need at least a chapter on its own. There are basically three ways of extending schemes to three dimensions which we will discuss separately below.

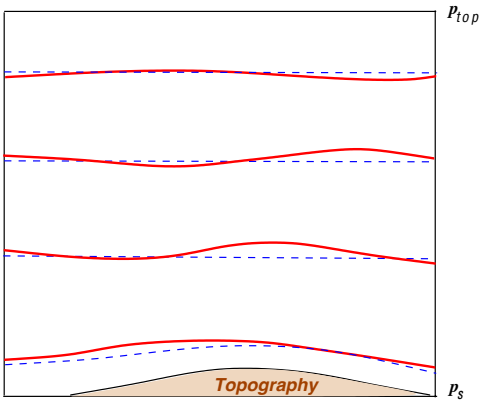

Fig. 8.18 A graphical illustration the floating Lagrangian coordinate. The vertical coordinate is pressure. p_s and p_{top} is the pressure at the surface and model top, respectively. The dashed lines is the reference Eulerian grid and solid lines are Lagrangian surfaces resulting from letting the Eulerian levels evolve in time, and require a periodic remapping.

8.6.1 Floating Lagrangian vertical coordinate

The floating Lagrangian coordinate was introduced in a theoretical context by Starr (1945) and first applied in discretized models over half a century later (e.g. Lin, 2004; Lauritzen et al, 2008; Nair et al, 2009). Instead of using vertical coordinates based on height or pressure, a vertical coordinate ζ that is constant along three-dimensional parcel trajectories is used

$$\frac{d\zeta}{dt} = 0, \tag{8.86}$$

(see Fig. 8.18). The benefit of using such a vertical coordinate is that the vertical advection terms in the equations of motion are eliminated and only two-dimensional transport/advection operators are necessary. The downside, as with any other Lagrangian approach, is that the vertical coordinate deform as the flow evolves. In order to avoid overly deformed vertical coordinates a remapping of the prognostic variables in the vertical to some reference vertical coordinate is necessary. This may be a source of vertical diffusion in the model. Note that isentropic vertical coordinates are a subset of floating Lagrangian vertical coordinates as they are also material surfaces for adiabatic flow.

8.6.2 Operator splitting

Using a cascade finite-volume scheme (flow based splitting) or Eulerian operator splitting the extension to three dimensions can be made less costly than when using fully three dimensional approaches simply because they require only one-dimensional operators. Eulerian type operator splitting use a combination of operators applied along coordinate lines (see, e.g., Pietrzak 1998). In such approaches errors due to the coordinate splitting (also referred to as splitting error) will appear if care is not taken to alleviate them. Various methods for reducing the splitting error have been proposed (e.g., Strang 1968, Lin and Rood 1996). The traditional Eulerian type operator splitting approach may be referred to as a fixed direction based splitting method as opposed to the flow-based splitting approach discussed below.

More recently the finite-volume cascade approach was suggested by Nair et al (2002) and Zerroukat et al (2002) which uses a combination of Eulerian and Lagrangian operators, that is, the operators are successively applied along coordinate lines and Lagrangian lines, respectively. So rather than being a fixed direction based splitting method it is flow-based (for a review see Machenhauer et al 2009). Since the splitting is flow-based the splitting error is reduced. Note that one may use the cascade approach to extend fully two-dimensional methods to three dimensions by applying a cascade sweep in the vertical based on the horizontally transported values.

8.6.3 Rigorous three-dimensional approach

Fully three-dimensional schemes based on the space-time finite-volume approach discussed in this chapter are rather complex. Instead of having to deal with overlap areas (as discussed in this chapter) one has to compute overlap volumes which is significantly complicating the problem. Examples of fully three-dimensional remapping algorithms are given in, e.g., Garimella et al (2007) for Cartesian geometry. The authors are not aware of any fully three-dimensional finite-volume remapping schemes on the sphere.

8.7 Time-integration and tracer transport

If all models would use the same numerical method for tracer transport as used for the continuity equation for air, and if those would always be solved by using the same time-step, then this section would be irrelevant. Most models, however, use one of the following three approaches: Either they use different schemes for air and tracers, use different time-step size for air and tracers (but explicit time-stepping for both) or semi-implicit time-stepping is used for air and explicit time-stepping for

tracers (and both use the same time-step). All of these approaches potentially have consistency problems as discussed separately for each approach below.

8.7.1 Different schemes air and tracers

If different schemes are used for air and tracers consistency cannot be achieved other than with fixers that enforce consistency in a 'ad hoc' and somewhat arbitrary manner. See section 8.3.4 and references therein.

8.7.2 Different time-steps for air and tracers (sub-cycling, super-cycling)

Given the increase in the number of prognostic tracers in atmospheric models, significant computational cost savings can be obtained by using a longer time-step for tracers than for the solution of the air continuity equation. As discussed in section 8.2.2 the maximum allowable time-step that can be used for the solution of the equation for air density (when using explicit time-stepping) is determined by the fastest wave in the system, since the continuity equation for air is directly coupled to the other equations of motion. The continuity equations for tracers, however, are not directly coupled (at least in terms of stability) to the momentum and thermodynamic equations and therefore have less restrictive time-step limitations. So a stable and more efficient integration scheme can be designed by sub-cycling the solution of the air density equation with respect to the tracer equations. In doing so it is important to retain the consistency discussed in section 8.2.2, that is, for a constant mixing ratio ($q = 1$) the tracer transport equation should yield the same solution as the continuity equation for air (a.k.a. 'free-stream preserving'). A scheme possessing the 'free-stream preserving' property can be designed as described below.

A conceptual explanation of sub-cycling is given with the aid of Fig. 8.19. For simplicity assume one spatial dimension, flow from left to right and that the wind at the right cell wall is zero (no mass flux through that boundary). The number of times the integration of the air density equation is sub-cycled with respect to the tracer equations is referred to as $ksplit$. In Fig. 8.19 $ksplit$ is 4. At time $t = n\Delta t$ the mass in the cell is ρ^n, where we have assumed that the cell width is one (grey area on Fig. 8.19a). We then integrate the full dynamical system of equations (continuity equation for air, momentum equations and thermodynamic equation) forward in time to $t = (n + 1/ksplit)\Delta t$. The flux of mass into the cell during this forward integration corresponds to the red area 'swept' through the left cell wall, on Fig. 8.19a (left column) and hence the air mass in the cell increases by the red area in cell k (Fig. 8.19a right column). This procedure is repeated three, or $(ksplit - 1)$, more time-steps during which the blue, yellow and green areas are 'swept' through the left cell wall and adding to the total air mass in the cell (Fig. 8.19b,c,d, respectively).

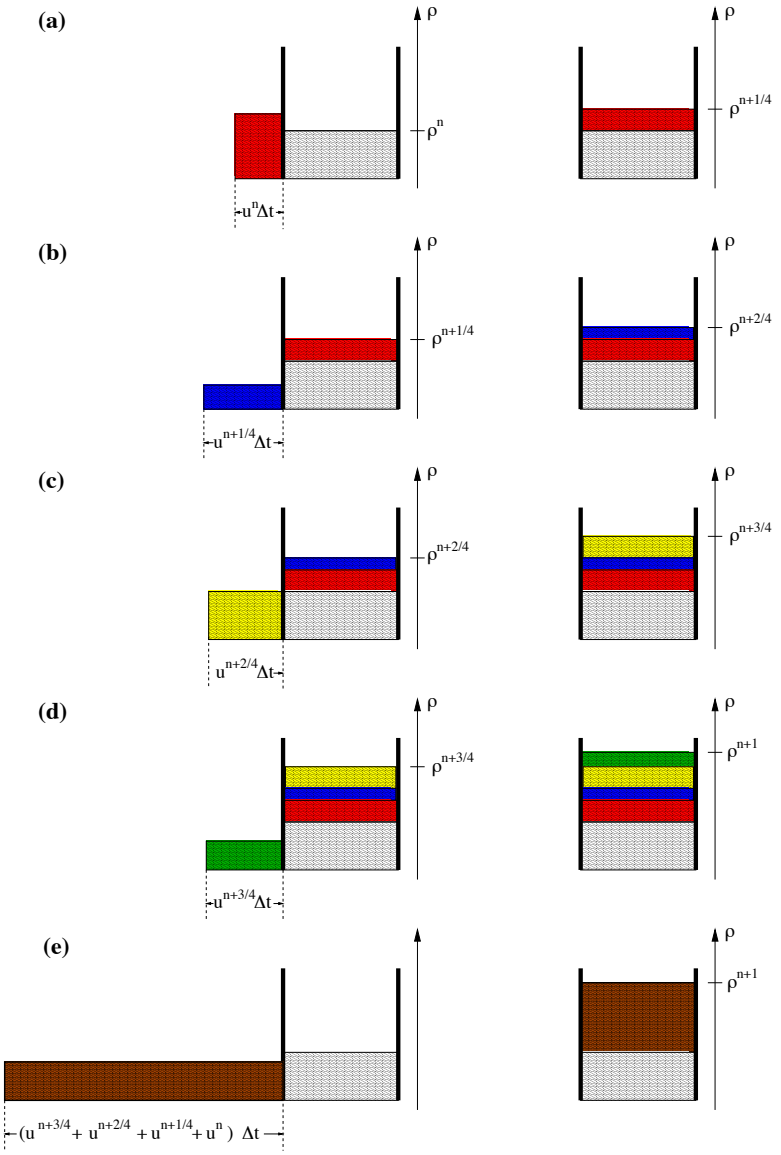

Fig. 8.19 A graphical illustration of sub-cycling the continuity for air mass with respect to tracers. Details and explanations are given in the text.

The total flow of mass into the cell is the sum of all the areas on Fig. 8.19a,c,b,d corresponding to an average flux into the cell given by the brown area on Fig. 8.19e.

Since we are updating tracers on the long time-step we use the transport scheme to estimate the average mixing ratio over the full time-step Δt, that is, the average

of q^n over the brown area in Fig. 8.19e denoted $\langle q^n \rangle$. Then the final forecast for the tracer is given by the product between the background flow of mass and an estimate of the mixing ratio over the long time-step

$$(\rho q)^{n+1} = (\rho q)^n + \langle q^n \rangle \left[\sum_{i=1}^{ksplit} \Delta \rho^{n+i/ksplit} \right], \tag{8.87}$$

where $\delta \rho^{n+i/ksplit}$ is the flux of air mass into the cell during one sub-cycled time-step $\Delta t/ksplit$. If $q = 1$ then (8.87) reduces to the equation for air mass and consequently the scheme is free-stream preserving. Note that updating the tracers on the short time-step will not yield the same result.

8.7.3 Semi-implicit time-stepping for air and explicit for tracers

If semi-implicit time-stepping is used (see chapter 6) then the prognostic equation for air density can be written as

$$\rho^{n+1} = \rho_{exp}^{n+1} + \frac{\Delta t}{2} \rho^{ref} \left(D^{n+1} - \tilde{D}^{n+1} \right), \tag{8.88}$$

(e.g. Lauritzen et al, 2006) where ρ_{exp}^{n+1} is the explicit prediction, ρ^{ref} is a constant reference density, D is the divergence and $\tilde{D}$ is the divergence extrapolated to time-level $n+1$. The terms on the right-hand side of (8.88) involving D are referred to as the semi-implicit correction terms and represent the implicit coupling to the momentum equations. If the tracer transport equation is solved explicitly, as is usually done, then the scheme is not 'free stream preserving' because of the semi-implicit correction terms (although they are usually small).

So for consistency, one should also solve the tracer transport equation semi-implicitly

$$(\rho q)^{n+1} = (\rho q)_{exp}^{n+1} + \frac{\Delta t}{2} (q\rho)^{ref} \left(D^{n+1} - \tilde{D}^{n+1} \right), \tag{8.89}$$

(e.g. Lauritzen et al, 2008), however, that seems problematic. For example, if q is zero in some area and the semi-implicit correction terms are non-zero in that area, then tracer mass will be produced in an area where q should be zero.

Thuburn et al (2010) present a method where they discretize an alternative form of the semi-implicit continuity equation. Through a series of iterations the semi-implicit correction terms cancel and consistency between air mass and tracer transport is obtained. For more details see Thuburn et al (2010).

8.8 Final Remarks

In this chapter a detailed discussion of desirable properties for transport schemes intended for meteorological applications has been presented. The finite-volume method for tracer transport (in two-dimensional Cartesian geometry) has been introduced and discussed using a remap approach which conceptually introduces the finite-volume method through following characteristics of the flow. This conceptual framework has been used to explain and analyze several schemes from the literature. Practical considerations related to the coupling of air mass equations and tracer mass equations has been discussed in some detail as well as brief introductions to extensions to spherical geometry and three dimensions. The authors hope to have communicated some of the aspects that go into modeling transport accurately in large modeling systems. Although physical parameterizations that represent sub-grid-scale processes are probably among the largest sources of uncertainty in weather and climate models, the accurate representation of transport is very important. Errors in resolved-scale transport can change scientific results (e.g. Rasch et al, 2006; Wild and Prather, 2006).

Acknowledgments Thanks to Dr. S. Galmarini (Institute for Environment and Sustainability, European Commission, Joint Research Center) and Dr. A. Baklanov (Danish Meteorological Institute) for details on the ETEX experiment. Many fruitful discussions with Dr. D.L. Williamson (NCAR), Dr. P. Rasch (PNNL), Dr. A.Gettelman (NCAR), Dr. W. Skamarock (NCAR), Dr. M. Taylor (Sandia National Laboratories) and Dr. R. Mittal (NCAR) are acknowledged as well as the internal review performed by Dr. D.L. Williamson and Dr. C. Erath, and the anonymous and Editor (Dr. C. Jablonowski and Dr. M.A. Taylor) reviews. The authors gratefully acknowledge Prof. J.Thuburn's suggestions on numerical mixing tests. The first and third authors were partially supported by the DOE BER Program under award DE-SC0001658.

References

van Albada GD, van Leer B, Roberts WW (1982) A comparative study of computational methods in cosmic gas dynamics. Astronomy and Astrophysics 108:76–84

Artebrant R, Torrilhon M (2008) Increasing the accuracy in locally divergence-preserving finite volume schemes for MHD. J Comput Phys 227(6):3405–3427

Barth T, Frederickson P (1990) Higher-order solution of the Euler equations on unstructured grids using quadratic reconstruction. In: AIAA Paper 90-0013

Barth T, Jespersen D (1989) The design and application of upwind schemes on unstructured meshes. Proc AIAA 27th Aerospace Sciences Meeting, Reno

Bates JR, McDonald A (1982) Multiply-upstream, semi-Lagrangian advective schemes: Analysis and application to a multi-level primitive equation model. Mon Wea Rev 110(12):1831–1842

Blossey PN, Durran DR (2008) Selective monotonicity preservation in scalar advection. J Comput Phys 227(10):5160–5183

Bockman SF (1989) Generalizing the formula for areas of polygons to moments. The American Mathematical Monthly 96:131–132

Brasseur GP, Hauglustaine DA, Walters S, Rasch PJ, Muller JF, Granier C, Tie XX (1998) MOZART, a global chemical transport model for ozone and related chemical tracers: 1. model description. J Geophys Res 103:28,265–28,289

Colella P, Sekora MD (2008) A limiter for ppm that preserves accuracy at smooth extrema. J Comput Phys 227:7069–7076

Colella P, Woodward PR (1984) The piecewise parabolic method (PPM) for gas-dynamical simulations. J Comput Phys 54:174–201

Collins WD, Rasch PJ, Boville BA, Hack JJ, McCaa JR, Williamson DL, Kiehl JT, Briegleb B (2004) Description of the NCAR Community Atmosphere Model (CAM 3.0). NCAR Tech. Note, NCAR/TN-464+STR

van Dop H, Addis R, Fraser G, Girardi F, Graziani G, Inoue Y, Kelly N, Klug W, Kulmala A, Nodop K, Pretel J (1998) Etex: A European tracer experiment; observations, dispersion modelling and emergency response. Atmospheric Environment 32:4089 – 4094

Doswell CAI (1984) A kinematic analysis of frontogenesis associated with a nondivergent vortex. J Atmos Sci pp 1242–1248

Dukowicz JK (1984) Conservative rezoning (remapping) for general quadrilateral meshes. J Comput Phys 54:411–424

Dukowicz JK, Baumgardner JR (2000) Incremental remapping as a transport/advection algorithm. J Comput Phys 160:318–335

Dukowicz JK, Kodis JW (1987) Accurate conservative remapping (rezoning) for arbitrary Lagrangian-Eulerian computations. SIAM Journal on Scientific and Statistical Computing 8(3):305–321

Durran DD (1999) Numerical Methods for Wave Equations in Geophysical Fluid Dynamics. Springer-Verlag

Eluszkiewicz J, Hemler RS, Mahlman JD, Bruhwiler L, Takacs LL (2000) Sensitivity of age-of-air calculations to the choice of advection scheme. J Atmos Sci 57:3185–3201

Galmarini S, Bianconi R, Addis R, Andronopoulos S, Astrup P, Bartzis JC, Bellasio R, Buckley R, Champion H, Chino M, D'Amours R, Davakis E, Eleveld H, Glaab H, Manning A, Mikkelsen T, Pechinger U, Polreich E, Prodanova M, Slaper H, Syrakov D, Terada H, der Auwera LV (2004) Ensemble dispersion forecasting–part II: Application and evaluation. Atmospheric Environment 38:4619 – 4632

Garimella R, Kucharik M, Shashkov M (2007) An efficient linearity and bound preserving conservative interpolation (remapping) on polyhedral meshes. Computers & Fluids 36:224 – 237

Girardi F, Graziani G, van Veltzen D, Galmarini S, Mosca S, Bianconi R, Bellasio R, Klug W (1998) The ETEX project. EUR report 181-43 en., Office for official publication of the European Communities, Luxembourg, 108 pp.

Godunov SK (1959) A difference scheme for numerical computation of discontinuous solutions of equations in fluid dynamics. Math Sb 47:271, also: Cornell Aero. Lab. translation

Haltiner GJ, Williams RT (1980) Numerical Prediction and Dynamic Meteorology. John Wiley & Sons, 477 pp.

Harris LM, Lauritzen PH, Mittal R (2010) A flux-form version of the conservative semi-Lagrangian multi-tracer transport scheme (CSLAM) on the cubed sphere grid. J Comput Phys In press

Harten A (1983) On the symmetric form of systems of conservation laws with entropy. J Comput Phys 49:151 – 164

Harten A, Engquist B, Osher S, Chakravarthy SR (1987) Uniformly high order accurate essentially non-oscillatory schemes iii. J Comput Phys 71:231–303

Hirt CW, Amsden AA, Cook JL (1974) An arbitrary Lagrangian-Eulerian computing method for all flow speeds. J Comput Phys 14(3):227 – 253

Hortal M (2002) The development and testing of a new two-time-level semi-Lagrangian scheme (SETTLS) in the ecmwf forecast model. Q J R Meteorol Soc 128(583):1671–1687

Jablonowski C, Lauritzen PH, Taylor MA, Nair RD (2010) Idealized test cases for the dynamical cores of atmospheric general circulation models. Geoscientific Model Development In prep. http://esse.engin.umich.edu/admg/publications.php

Jöckel P, von Kuhlmann R, Lawrence MG, Steil B, Brenninkmeijer C, Crutzen PJ, Rasch PJ, Eaton B (2001) On a fundamental problem in implementing flux-form advection schemes for tracer transport in 3-dimensional general circulation and chemistry transport models. QJR Meteorol Soc 127(573):1035–1052

Jones PW (1999) First- and second-order conservative remapping schemes for grids in spherical coordinates. Mon Wea Rev 127:2204–2210

Lamarque JF, Kinnison DE, Hess PG, Vitt F (2008) Simulated lower stratospheric trends between 1970 and 2005: Identifying the role of climate and composition changes. J Geophys Res 113(D12301)

Laprise JP, Plante A (1995) A class of semi-Lagrangian integrated-mass (SLIM) numerical transport algorithms. Mon Wea Rev 123:553–565

Lauritzen PH (2007) A stability analysis of finite-volume advection schemes permitting long time steps. Mon Wea Rev 135:2658–2673

Lauritzen PH, Nair RD (2008) Monotone and conservative cascade remapping between spherical grids (CaRS): Regular latitude-longitude and cubed-sphere grids. Mon Wea Rev 136:1416–1432

Lauritzen PH, Thuburn J (2010) Evaluating advection/transport schemes using scatter plots and numerical mixing diagnostics. Quart J Roy Met Soc In prep

Lauritzen PH, Kaas E, Machenhauer B (2006) A mass-conservative semi-implicit semi-Lagrangian limited area shallow water model on the sphere. Mon Wea Rev 134:1205–1221

Lauritzen PH, Kaas E, Machenhauer B, Lindberg K (2008) A mass-conservative version of the semi-implicit semi-Lagrangian HIRLAM. QJR Meteorol Soc 134

Lauritzen PH, Nair RD, Ullrich PA (2010) A conservative semi-Lagrangian multi-tracer transport scheme (CSLAM) on the cubed-sphere grid. J Comput Phys 229:1401–1424

Lee SM, Yoon SC, Byun DW (2004) The effect of mass inconsistency of the meteorological field generated by a common meteorological model on air quality modeling. Atmospheric Environment 38(18):2917 – 2926

van Leer B (1977) Towards the ultimate conservative difference scheme. IV: A new approach to numerical convection. J Comput Phys 23:276–299

Leonard BP (1991) The ULTIMATE conservative difference scheme applied to unsteady one-dimensional advection. Comput Methods Appl Mech Eng 88:17–74

Leonard BP, Lock A, MacVean M (1996) Conservative explicit unrestricted-time-step multidimensional constancy-preserving advection schemes. Mon Wea Rev 124:2588–2606

Leslie LM, Dietachmayer GS (1997) Comparing schemes for integrating the Euler equations. Mon Wea Rev 125(7):1687–1691

LeVeque RJ (1996) High-resolution conservative algorithms for advection in incompressible flow. SIAM Journal on Numerical Analysis 33:627–665

Levy MN, Nair RD, Tufo HM (2007) High-order Galerkin method for scalable global atmospheric models. Comput Geosci 33:1022–1035

Lin SJ (2004) A 'vertically Lagrangian' finite-volume dynamical core for global models. Mon Wea Rev 132:2293–2307

Lin SJ, Rood RB (1996) Multidimensional flux-form semi-Lagrangian transport schemes. Mon Wea Rev 124:2046–2070

Lipscomb WH, Ringler TD (2005) An incremental remapping transport scheme on a spherical geodesic grid. Mon Wea Rev 133:2335–2350

Liu Y, wang Shu C, Tadmor E, Zhang M (2007) Central discontinuous Galerkin methods on overlapping cells with a non-oscillatory hierarchical reconstruction. SIAM J Numer Anal pp 45–2442

Lorenz EN (1982) Atmospheric predictability experiments with a large numerical model. Tellus pp 505–513

Machenhauer B, Kaas E, Lauritzen PH (2009) Finite volume methods in meteorology, in: R. Temam, J. Tribbia, P. Ciarlet (Eds.), Computational methods for the atmosphere and the oceans. Handbook of Numerical Analysis 14, Elsevier, 2009, pp.3-120

McGregor JL (2005) Geostrophic adjustment for reversibly staggered grids. Mon Wea Rev 133:1119–1128

Miura H (2007) An upwind-biased conservative advection scheme for spherical hexagonal-pentagonal grids. Mon Wea Rev 135:4038–4044

Moorthi S, Higgins RW, Bates JR (1995) A global multilevel atmospheric model using a vector semi-Lagrangian finite-difference scheme. Part II: Version with physics. Mon Wea Rev 123(5):1523–1541

Morrison H, Gettelman A (2008) A new two-moment bulk stratiform cloud microphysics scheme in the community atmosphere model, version 3 (CAM3). Part I: Description and numerical tests. J Climate 21:3642–3659

Nair RD, Jablonowski C (2008) Moving vortices on the sphere: A test case for horizontal advection problems. Mon Wea Rev 136:699–711

Nair RD, Lauritzen PH (2010) A class of deformational flow test cases for linear transport problems on the sphere. J Comput Phys 229:8868–8887

Nair RD, Machenhauer B (2002) The mass-conservative cell-integrated semi-Lagrangian advection scheme on the sphere. Mon Wea Rev 130(3):649–667

Nair RD, Scroggs JS, Semazzi FHM (2002) Efficient conservative global transport schemes for climate and atmospheric chemistry models. Mon Wea Rev 130(8):2059–2073

Nair RD, Choi HW, Tufo HM (2009) Computational aspects of a scalable high-order discontinuous Galerkin atmospheric dynamical core. Computers & Fluids 38:309–319

Norman MR, Nair RD (2008) Inherently conservative nonpolynomial-based remapping schemes: Application to semi-Lagrangian transport. Mon Wea Rev 126:5044–5061

Norman MR, Semazzi FHM, Nair RD (2009) Conservative cascade interpolation on the sphere: An intercomparison of various non-oscillatory reconstructions. Quart J Roy Met Soc 135:795–805

Ovtchinnikov M, Easter RC (2009) Nonlinear advection algorithms applied to interrelated tracers: Errors and implications for modeling aerosol-cloud interactions. Mon Wea Rev 137:632–644

Pietrzak J (1998) The use of TVD limiters for forward-in-time upstream-biased advection schemes in ocean modeling. Mon Wea Rev 126:812–830

Plumb RA (2007) Tracer interrelationships in the stratosphere. Rev Geophys 45(RG4005)

Plumb RA, Ko M (1992) Interrelationships between mixing ratios of long-lived stratospheric constituents. J Geophys Res 97:10,145–10,156

Prather MJ, Zhu X, Strahan SE, Steenrod SD, Rodriguez JM (2008) Quantifying errors in trace species transport modeling. Proceedings of the National Academy of Science pp 19,617–19,621

Purser RJ, Leslie LM (1991) An efficient interpolation procedure for high-order three-dimensional semi-Lagrangian models. Mon Wea Rev 119:2492–2498

Putman WM, Lin SJ (2007) Finite-volume transport on various cubed-sphere grids. J Comput Phys 227(1):55–78

Rančić M (1992) Semi-Lagrangian piecewise biparabolic scheme for two-dimensional horizontal advection of a passive scalar. Mon Wea Rev 120:1394–1405

Rasch PJ, Coleman DB, Mahowald N, Williamson DL, Lin SJ, Boville BA, Hess P (2006) Characteristics of atmospheric transport using three numerical formulations for atmospheric dynamics in a single GCM framework. J Climate 19:2243–2266

Roe PL (1985) Lecture Notes in Applied Mathematics, vol 22, New York: Springer-Verlag, chap Some contributions to modeling of discontinuous flows, pp 163–193

Rood RB (1987) Numerical advection algorithms and their role in atmospheric transport and chemistry models. Rev Geophys 25:71–100

Schär C, Smolarkiewicz PK (1996) A synchronous and iterative flux-correction formalism for coupled transport equations. J Comput Phys 128:101–120

Smolarkiewicz PK (2006) Multidimensional positive definite advection transport algorithm: An overview. Int J Numer Methods Fluids 50:1123–1144

Smolarkiewicz PK, Grabowski WW (1990) The multidimensional positive definite advection transport algorithm: Nonoscillatory option. J Comput Phys 86:355 – 375

Staniforth A, Côté J (1991) Semi-Lagrangian integration schemes for atmospheric models-a review. Mon Wea Rev 119:2206–2223

Staniforth A, White A, Wood N (2003) Analysis of semi-Lagrangian trajectory computations. Q J R Meteorol Soc 129(591):2065–2085

Starr VP (1945) A quasi-Lagrangian system of hydrodynamical equations. J Atmos Sci 2:227–237

Strang G (1968) On the construction and comparison of difference schemes. SIAM J Numer Anal 5:506–517

Thuburn J (2008) Some conservation issues for the dynamical cores of NWP and climate models. J Comput Phys 227:3715 – 3730

Thuburn J, Mclntyre M (1997) Numerical advection schemes, cross-isentropic random walks, and correlations between chemical species. J Geophys Res 102(D6):6775–6797

Thuburn J, Zerroukat M, Wood N, Staniforth A (2010) Coupling a mass conserving semi-Lagrangian scheme (SLICE) to a semi-implicit discretization of the shallow-water equations: Minimizing the dependence on a reference atmosphere. Q J R Meteorol Soc 136:146–154

Toro EF (1999) Riemann Solvers and Numerical Methods for Fluid Dynamics, Second edn. Springer, ISBN-10: 3540659668, 624 pp.

Trenberth KE, Smith L (2005) The mass of the atmosphere: A constraint on global analyses. J Climate 18:864–875

Ullrich PA, Lauritzen PH, Jablonowski C (2009) Geometrically exact conservative remapping (GECoRe): Regular latitude-longitude and cubed-sphere grids. Mon Wea Rev 137(6):1721–1741

Ullrich PA, Jablonowski C, van Leer BL (2010) Riemann-solver-based high-order finite-volume models for the shallow-water equations on the sphere. J Comput Phys 229:6104–6134

Waugh DW, Hall TM (2002) Age of stratospheric air: Theory, observations, and models. Rev Geophys 40

Waugh DW, Plumb RA, Elkins JW, Fahey DW, Boering KA, Dutton GS, Volk CM, Keim E, Gao RS, Daube BC, Wofsy SC, Loewenstein M, Podolske JR, Chan KR, Proffitt MH, Kelly KK, Newman PA, Lait LR (1997) Mixing of polar vortex air into middle latitudes as revealed by tracer-tracer scatterplots. J Geophys Res 120(D11):119–134

White L, Adcroft A (2008) A high-order finite volume remapping scheme for nonuniform grids: The piecewise quartic method (PQM). J Comput Phys 227:7394 – 7422

Wild O, Prather MJ (2006) Global tropospheric ozone modeling: Quantifying errors due to grid resolution. J Geophys Res 111(D11305)

Williamson DL, Olson J (1994) Climate simulations with a semi-Lagrangian version of the NCAR Community Climate Model. Mon Wea Rev 122(7):1594–1610

Williamson DL, Drake JB, Hack JJ, Jakob R, Swarztrauber PN (1992) A standard test set for numerical approximations to the shallow water equations in spherical geometry. J Comput Phys 102:211–224

Xiao F, Yabe T, Peng X, Kobayashi H (2002) Conservative and oscillation-less atmospheric transport schemes based on rational functions. J Geophys Res 107(D22):4609

Yabe T, Tanaka R, Nakamura T, Xiao F (2001) An exactly conservative semi-Lagrangian scheme (cip csl) in one dimension. Mon Wea Rev 129(2):332–334

Yeh KS (2007) The streamline subgrid integration method: I. quasi-monotonic second-order transport schemes. J Comput Phys 225:1632 – 1652

Zalesak ST (1979) Fully multidimensional flux-corrected transport algorithms for fluids. J Comput Phys 31:335–362

Zerroukat M, Wood N, Staniforth A (2002) SLICE: A semi-Lagrangian inherently conserving and efficient scheme for transport problems. Q J R Meteorol Soc 128:2801–2820

Zerroukat M, Wood N, Staniforth A (2004) SLICE-S: A semi-Lagrangian inherently conserving and efficient scheme for transport problems on the sphere. Q J R Meteorol Soc 130:2649–2664

Zerroukat M, Wood N, Staniforth A (2005) A monotonic and positive-definite filter for a semi-Lagrangian inherently conserving and efficient (SLICE) scheme. Q J R Meteorol Soc 131(611):2923–2936

Zerroukat M, Wood N, Staniforth A (2006) The parabolic spline method (PSM) for conservative transport problems. Int J Numer Meth Fluids 51:1297–1318

Zerroukat M, Wood N, Staniforth A (2007) Application of the parabolic spline method (PSM) to a multi-dimensional conservative semi-Lagrangian transport scheme (SLICE). J Comput Phys 225:935–948

Zerroukat M, Staniforth A, Wood N (2010) The monotonic quartic spline method (QSM) for conservative transport problems. J Comput Phys 229:1150 – 1166

Zhang K, Wan H, Wang B, Zhang M (2008) Consistency problem with tracer advection in the atmospheric model GAMIL. Adv Atmos Sci 25(2)

Zubov VA, Rozanov EV, Schlesinger ME (1999) Hybrid scheme for three-dimensional advective transport. Mon Wea Rev 127(6):1335–1346